*J. Applied Membrane Science & Technology*, Vol. 30, August 2026, 198-230


# Statistically-assisted Optimization of PVDF-MWCNT-Triclosan Hybrid Membrane for High Flux, Salt Rejection, and Contact Angle

**D. Md Sukor[1,2], R. A. Wahab[1,2] & N. Yusmaidi[1]**

[1]Department of Chemistry, Faculty of Science, Universiti Teknologi Malaysia, 81310 UTM Johor Bahru, Johor, Malaysia
[2]Microplastic Research Interest Group (MRIG), Faculty of Science and Marine Environment, Universiti Malaysia Terengganu, 21030, Kuala Nerus, Terengganu, Malaysia

Submitted: 01/07/2026. Revised edition: 06/08/2026. Accepted: 06/08/2026. Available online: 21/08/2026

## ABSTRACT

Membrane distillation offers a promising solution for water desalination, yet its broader application is severely hindered by biofouling and membrane wetting. To address these limitations, this study developed a novel polyvinylidene fluoride (PVDF) membrane enhanced with multi-walled carbon nanotubes (MWCNTs) and silica nanoparticles ($SiO_2$), cross-linked with epichlorohydrin (ECH), and coated with the antimicrobial agent triclosan (TCS), aimed at improving hydrophobicity and anti-biofouling properties. The membrane was fabricated via phase inversion and optimized using Response Surface Methodology with a Box-Behnken design across 17 experimental runs. Qualitatively, ATR-FTIR spectroscopy confirmed the successful incorporation of MWCNT (C=O ester at 1733.04 $cm^{-1}$), TCS (aromatic C=C at 1639.70 and 1452.91 $cm^{-1}$), and $SiO_2$ (Si–O–Si at 1070.80 $cm^{-1}$), while SEM revealed a porous cross-section with pore sizes reduced from ~450 nm to ~200 nm after TCS coating. Quantitatively, the optimal membrane (2 wt.% ECH, 1 wt.% TCS, 2 wt.% $SiO_2$) achieved a contact angle of 92.98°, a water flux of 11.05 $kg \cdot m^{-2} \cdot h^{-1}$, and a salt rejection of 75.36%, with total porosity reaching 82.40%. The findings demonstrate that TCS functionalization successfully enhances hydrophobicity and flux, though salt rejection remains below industrial benchmarks. Further optimization of TCS dispersion and membrane formulation is necessary to achieve superhydrophobic performance (>150° contact angle) and >99% salt rejection for practical desalination applications.

*Keywords: Multiwalled carbon nanotubes; triclosan; PVDF; statistically-optimized; membrane distillation; desalination*

## 1.0 INTRODUCTION

Global freshwater scarcity has emerged as one of the most pressing challenges of the 21st century, driven by population growth, industrialization, climate change, and the unsustainable exploitation of existing water resources [1]. With approximately 2.2 billion people worldwide lacking access to safely managed drinking water, the development of

* Corresponding to: R. A. Wahab (email: roswanira@utm.my)
DOI: https://doi.org/10.11113/jamst.v30n2.353

reliable and sustainable desalination technologies has become critically urgent for recovering water from saline sources, industrial wastewater, and agricultural runoff [2]. Among the various desalination technologies, membrane distillation (MD) has garnered significant research attention as a thermally driven separation process that combines the advantages of membrane separation and thermal distillation [3]. Unlike pressure-driven processes such as reverse osmosis (RO), MD operates on the principle of vapour pressure difference across a hydrophobic microporous membrane, enabling theoretically 100% rejection of non-volatile solutes while utilizing low-grade heat sources, including solar energy, geothermal energy, or industrial waste heat [4]. Direct contact membrane distillation (DCMD), the most widely studied configuration, involves direct contact between the heated feed solution and the cold permeate stream, offering operational simplicity and high flux under optimal conditions [5].

Despite its promising attributes, the industrial implementation of MD remains limited due to two critical challenges: membrane wetting and fouling [6]. Membrane wetting occurs when the feed liquid penetrates the hydrophobic membrane pores, blocking vapor transport pathways and causing a precipitous decline in both flux and salt rejection [7]. This phenomenon becomes particularly severe in the presence of low-surface-tension contaminants such as oils, surfactants, and organic compounds, which reduce the liquid entry pressure and accelerate irreversible pore wetting [8]. Concurrently, membrane fouling, the accumulation of inorganic scales, organic matter, and biological substances on the membrane surface or within its pore structure, increases heat and mass transfer resistance, leading to rapid flux decline and performance deterioration [9]. The interplay between wetting and fouling creates a synergistic effect that severely compromises membrane longevity and separation efficiency, necessitating the development of advanced membrane materials with enhanced anti-wetting and anti-fouling properties [10].

Polyvinylidene fluoride (PVDF) has emerged as a preferred membrane material for MD applications due to its excellent thermal stability, chemical resistance, mechanical strength, and inherent hydrophobicity [11]. However, the intrinsic hydrophobicity of PVDF, while essential for vapour passage, also promotes hydrophobic–hydrophobic interactions with organic foulants, exacerbating biofouling through the adhesion of proteins, humic substances, and microorganisms [12]. To overcome these limitations, researchers have explored various modification strategies to enhance membrane hydrophobicity and, ideally, impart superhydrophobic characteristics, defined by water contact angles exceeding 150° and low sliding angles, thereby creating protective air pockets that minimize liquid-membrane contact and reduce fouling propensity [13]. However, achieving such extreme hydrophobicity requires careful optimization of surface chemistry and morphology [13]. Likewise, the incorporation of nanoparticles such as silica ($SiO_2$), titanium dioxide ($TiO_2$), and carbon-based nanomaterials has proven effective in increasing surface roughness and creating hierarchical micro-nano structures that promote superhydrophobicity [14]. For instance, $SiO_2$ nanoparticles have been extensively utilized to confer superhydrophobic properties to PVDF membranes, with silanized $SiO_2$-modified PVDF membranes achieving contact angles exceeding 150° and demonstrating enhanced water flux and reduced flux decline [15].

Multi-walled carbon nanotubes (MWCNTs) offer additional advantages for membrane modification, including exceptional mechanical properties, high aspect ratios, and the ability to enhance vapour flux in polymeric matrices [16]. MWCNT-embedded PVDF

* Corresponding to: R. A. Wahab (email: roswanira@utm.my)
DOI: https://doi.org/10.11113/jamst.v30n2.353

membranes have shown improved hydrophobicity, porosity, and anti-fouling performance, attributed to the formation of nanoscale roughness and preferential pathways for water vapour transport [17]. However, the inherent tendency of MWCNTs to agglomerate through van der Waals forces necessitate functionalization strategies to ensure homogeneous dispersion and maximize their beneficial effects [18]. The synergistic integration of MWCNTs and $SiO_2$ nanoparticles has demonstrated remarkable potential in creating robust composite structures that simultaneously enhance hydrophobicity, mechanical strength, and anti-fouling resistance [19].

Beyond physical anti-fouling approaches, incorporating antibacterial agents offers a complementary strategy to mitigate biofouling, the growth of bacteria, fungi, and algae that form irreversible biofilms on membrane surfaces [20]. Triclosan (TCS), a halogenated biphenyl ether recognized for its broad-spectrum antimicrobial activity, has been widely employed as an organic biocide in personal care products, medical devices, and surface coatings [21]. Unlike metallic biocides that may leach toxic ions, TCS offers the advantage of stable covalent immobilization, providing sustained antibacterial activity without releasing hazardous compounds [22]. Recent studies have demonstrated the successful immobilization of TCS onto polyamide thin-film composite membranes, achieving excellent antibacterial activity against both Gram-negative and Gram-positive bacteria while maintaining high separation performance [23]. The covalent attachment of TCS to functionalized MWCNTs via cross-linking agents such as epichlorohydrin (ECH) represents a promising approach to create dual-functional membranes that combine superior hydrophobicity with robust antibacterial properties [24]. The process can be improved by statistically optimizing the multi-component membrane formulations. That said, Response Surface Methodology (RSM), particularly the Box-Behnken design (BBD), has proven to be an efficient statistical tool for modeling and optimizing membrane fabrication parameters while minimizing the number of experimental runs [25]. BBD enables assessment of individual factor effects and their interactions, facilitating the identification of optimal conditions to achieve desired performance metrics, including contact angle, water flux, and salt rejection [26].

In this context, the present study aims to develop a statistically optimized PVDF membrane enhanced with MWCNTs, $SiO_2$ nanoparticles, cross-linked with ECH, and functionalized with TCS for high-performance DCMD desalination, with the goal of improving hydrophobicity, flux, and salt rejection. While previous studies have individually explored the use of MWCNTs [17], $SiO_2$ nanoparticles [15], or TCS [23] for membrane modification, the covalent integration of TCS with MWCNT-ECH functionalized PVDF membranes represents a novel approach that combines enhanced hydrophobicity with sustained antibacterial activity. This dual-functional strategy addresses the persistent challenge of biofouling in membrane distillation, which remains a key obstacle to long-term operational stability [9, 20]. Although achieving superhydrophobicity (>150°) and >99% salt rejection is the ultimate goal, the present work provides a foundational framework for understanding the interactions between these components and their collective influence on membrane performance. The statistical optimization approach using RSM-BBD offers valuable insights into the optimal formulation ranges and interaction effects, which can guide future efforts to achieve industrial benchmarks. Hypothetically, the systematic integration of these components-MWCNTs for mechanical reinforcement and hydrophobicity enhancement, $SiO_2$ for

* Corresponding to: R. A. Wahab (email: roswanira@utm.my)
DOI: https://doi.org/10.11113/jamst.v30n2.353

hierarchical surface structuring, ECH for covalent cross-linking, and TCS for antibacterial protection—could address the multifaceted challenges of membrane wetting and biofouling. The novelty of this work lies in the covalent attachment of TCS to MWCNT-ECH functionalized PVDF membranes, creating a dual-functional system that combines enhanced hydrophobicity with sustained antibacterial activity, a combination not previously reported for DCMD applications. Through RSM-BBD optimization and comprehensive physicochemical characterization, this work aims to identify an optimal membrane formulation that maximizes contact angle, water flux, and salt rejection, thereby advancing membrane distillation technology for sustainable water treatment applications. The key takeaway from this study is that the synergistic integration of MWCNTs, $SiO_2$, and TCS, statistically optimized via RSM, can significantly enhance membrane performance, though further refinement is needed to meet industrial benchmarks.

## 2.0 EXPERIMENTAL

### 2.1 Materials

Polyvinylidene fluoride (PVDF, Mw ≈ 534,000, 99.5% purity) was purchased from Sigma-Aldrich (USA). Functionalised multi-walled carbon nanotubes (MWCNT-COOH, >95% purity, outer diameter 10–20 nm, length 10–30 μm) were obtained from Usains (Malaysia). Silica 60 ($SiO_2$, particle size 0.040–0.063 mm) was supplied by Macherey-Nagel (Germany). Epichlorohydrin (ECH, ≥99%), triclosan (TCS, 99%), N,N-dimethylacetamide (DMAc, 99%), polyethylene glycol (PEG, 99.5%), and lithium chloride (LiCl) were obtained from Sigma-Aldrich, Vchem, and RCl Labscan, as detailed in Table 1. All chemicals were used as received without further purification. Deionized water (18.2 MΩ·cm) was produced using a Milli-Q Advantage A10 system (Merck Millipore, USA) and used for all aqueous preparations.

**Table 1**. List of chemicals

| Chemicals | Source | Purity (%) |
|---|---|---|
| Polyvinylidene fluoride (PVDF) | Sigma–Aldrich | 99.5% |
| Functionalised multi-walled carbon nanotube (MWCNT) | Usains | - |
| Silica 60 ($SiO_2$) | Macherey-Nagel | - |
| Epichlorohydrin (ECH) | Aldrich Chemistry | ≥99% |
| Triclosan (TCS) | Sigma–Aldrich | 99% |
| N,*N*-Dimethylacetamide (DMAc) | Vchem | 99% |
| Lithium Chloride (LiCl) | LL Specialty Chemicals | - |
| Polyethylene Glycol (PEG) | RCl Labscan | 99.5% |

* Corresponding to: R. A. Wahab (email: roswanira@utm.my)
DOI: https://doi.org/10.11113/jamst.v30n2.353

## 2.2 Membrane Fabrication

### *2.2.1 Preparation of MWCNT/$SiO_2$/ECH-PVDF Dope Solutions*

The MWCNT/$SiO_2$/ECH-PVDF dope solutions were prepared using the phase inversion method, a well-established technique for fabricating porous polymeric membranes with controllable morphology and high reproducibility [13, 27]. Seventeen distinct dope formulations were prepared with varying concentrations of ECH (1.0–3.0 wt.%), $SiO_2$ (0.5–3.5 wt.%), and MWCNT (fixed at 0.255 wt.%), while the concentrations of PVDF (15 wt.%), LiCl (5 wt.%), and PEG (3 wt.%) were maintained constant across all formulations. The composition of each formulation is presented in Table 2. The preparation procedure commenced by dissolving PVDF in DMAc in a three-necked round-bottom flask placed in a thermostatted oil bath maintained at 50 ± 0.5 °C. The mixture was subjected to continuous magnetic stirring at 400 rpm for 12 h until a homogeneous and transparent solution was obtained. Following complete dissolution, LiCl and PEG were sequentially added to the solution, with continued stirring for an additional 4 h to ensure thorough mixing. Subsequently, MWCNT was added to the mixture and stirred for 2 h, after which $SiO_2$ and ECH were incorporated at the prescribed concentrations and stirred for a further 4 h. To achieve homogeneous dispersion of the nanoparticles and prevent agglomeration, the mixture was ultrasonicated in a bath using an Elmasonic P 120H at 80 W and 37 kHz for 30 min at room temperature. The resulting dope solution was then degassed by allowing it to stand at room temperature for 6 h, a critical step to eliminate entrapped air bubbles that could otherwise compromise the integrity of the membrane structure by creating pinhole defects during casting [28].

**Table 2.** Dope formulation of the MWCNT/$SiO_2$/ECH -PVDF membrane

| Dope | ECH (wt. %) | $SiO_2$ (wt. %) | MWCNT (wt. %) | PVDF (wt. %) | LiCl (wt. %) | PEG (wt. %) | DMAC (wt. %) |
|---|---|---|---|---|---|---|---|
| **1** | 1 | 2.0 | 0.255 | 15 | 5 | 3 | 73.745 |
| **2** | 3 | 2.0 | 0.255 | 15 | 5 | 3 | 71.745 |
| **3** | 1 | 2.0 | 0.255 | 15 | 5 | 3 | 73.745 |
| **4** | 3 | 2.0 | 0.255 | 15 | 5 | 3 | 71.745 |
| **5** | 1 | 0.5 | 0.255 | 15 | 5 | 3 | 75.245 |
| **6** | 3 | 0.5 | 0.255 | 15 | 5 | 3 | 73.245 |
| **7** | 1 | 3.5 | 0.255 | 15 | 5 | 3 | 72.245 |
| **8** | 3 | 3.5 | 0.255 | 15 | 5 | 3 | 70.245 |
| **9** | 2 | 0.5 | 0.255 | 15 | 5 | 3 | 74.245 |
| **10** | 2 | 0.5 | 0.255 | 15 | 5 | 3 | 74.245 |
| **11** | 2 | 3.5 | 0.255 | 15 | 5 | 3 | 71.245 |
| **12** | 2 | 3.5 | 0.255 | 15 | 5 | 3 | 71.245 |
| **13** | 2 | 2.0 | 0.255 | 15 | 5 | 3 | 72.745 |
| **14** | 2 | 2.0 | 0.255 | 15 | 5 | 3 | 72.745 |
| **15** | 2 | 2.0 | 0.255 | 15 | 5 | 3 | 72.745 |
| **16** | 2 | 2.0 | 0.255 | 15 | 5 | 3 | 72.745 |
| **17** | 2 | 2.0 | 0.255 | 15 | 5 | 3 | 72.745 |

* Corresponding to: R. A. Wahab (email: roswanira@utm.my)
DOI: https://doi.org/10.11113/jamst.v30n2.353

### *2.2.2 Membrane Casting and Phase Inversion*

The degassed dope solution was cast onto a clean, dry glass substrate using a stainless steel rod equipped with a 200 μm wire-wound applicator (Baker applicator, RK Print-Coat Instruments, UK) at a controlled casting speed of 5 cm/s. The casting procedure was conducted in a temperature-controlled environment maintained at 25 ± 0.5 °C with relative humidity below 60% to ensure consistent solvent evaporation kinetics and reproducibility across all experimental runs. Immediately after casting, the glass substrate bearing the polymer film was immersed in a coagulation bath containing 10 L of tap water at 25 ± 1 °C, where it remained for 24 h to allow complete phase inversion. During this period, the exchange of the solvent (DMAc) and the non-solvent (water) induced precipitation of the polymer, resulting in a porous membrane structure. The solidified membrane was then carefully peeled from the glass substrate and washed five times with deionized water to remove any residual DMAc and LiCl. The resulting membrane, designated as MWCNT/$SiO_2$/ECH-PVDF and hereafter referred to as the "XTCS membrane," was stored in deionized water at 4 °C for subsequent use and characterization.

### *2.2.3 Triclosan Coating of the Membrane*

The XTCS membrane was surface-modified with triclosan (TCS) following a procedure adapted from Sun *et al*. [29], with modifications to enhance coating uniformity and adhesion. TCS solutions were prepared at three distinct concentrations (0.3, 1.0, and 1.7 wt.%) by dissolving the appropriate mass of TCS in tris buffer solution (10 mM, pH 8.5) with continuous stirring at 60 °C for 1 h until complete dissolution was achieved. Membrane sections measuring 5 cm × 5 cm were cut from each XTCS membrane and immersed in 15 mL of the TCS solution contained within a 50 mL glass vessel. The vessels were then placed on an orbital shaker (Heidolph Rotamax 120) and agitated at 100 rpm for 24 h at room temperature to facilitate TCS deposition onto the membrane surface. Following the coating period, the TCS-modified membranes were thoroughly rinsed with deionized water (five times, 50 mL each) to remove any loosely bound or unreacted TCS from the surface. The rinsed membranes were then air-dried overnight at 25 °C in a dust-free cabinet and subsequently stored in sealed containers at 4 °C until further characterization. The resulting membrane was designated as MWCNT/$SiO_2$/ECH/TCS-PVDF and is hereafter referred to as the "TCS membrane."

## 2.3 Experimental Design and Statistical Optimization

A Box–Behnken Design (BBD) was employed using Design-Expert software (Version 13.0.5.0, Stat-Ease Inc., USA) to investigate the individual and interactive effects of three independent factors on the membrane performance responses. The BBD was selected over the alternative Central Composite Design (CCD) due to its operational advantages, including the requirement for fewer experimental runs (17 versus 20 for CCD with three factors), efficient estimation of quadratic model coefficients, and avoidance of extreme axial points that often represent impractical or unstable operating conditions in membrane fabrication processes [25, 30].

* Corresponding to: R. A. Wahab (email: roswanira@utm.my)
DOI: https://doi.org/10.11113/jamst.v30n2.353

The three independent factors investigated in this study were ECH concentration (1.0–3.0 wt.%), TCS concentration (0.3–1.7 wt.%), and $SiO_2$ concentration (0.5–3.5 wt.%), each examined at three coded levels: -1 (low), 0 (center), and +1 (high) (Table 3). The responses measured to evaluate membrane performance were contact angle (°), water flux ($kg \cdot m^{-2} \cdot h^{-1}$), and salt rejection (%). The complete experimental design comprised 17 runs, consisting of 12 factorial points and 5 center points, the latter being included to estimate pure experimental error. All runs were performed in randomized order to minimize the influence of systematic bias and time-dependent variability. The relationship between the responses and the independent variables was modeled using a second-order polynomial equation:

$$Y = \beta_0 + \sum_{i=1}^{3} \beta_i X_i + \sum_{i=1}^{3} \beta_{ii} X_i^2 + \sum_{i=1}^{2} \sum_{j=i+1}^{3} \beta_{ij} X_i X_j + \varepsilon \quad (1)$$

where Y represents the predicted response, $\beta_0$ is the intercept term, $\beta_i$ are the linear coefficients, $\beta_{ii}$ are the quadratic coefficients, $\beta_{ij}$ are the interaction coefficients, $X_i$ are the coded factor levels, and $\varepsilon$ is the random error term. Optimization was performed in this study using the desirability function approach, which transforms each response into a dimensionless desirability value ($d_i$) ranging from 0 (undesirable) to 1 (highly desirable). The overall desirability (D) is calculated as the geometric mean of the individual desirabilities: $D = (d_1 \times d_2 \times \ldots \times d_n)^{(1/n)}$. The optimization goal was to maximize all three responses, with equal weight assigned to each. The formulation with the highest overall desirability was selected as the optimal condition.

The adequacy of the fitted models was evaluated through comprehensive statistical diagnostics, including analysis of variance (ANOVA), the coefficient of determination ($R^2$), adjusted $R^2$, predicted $R^2$, adequate precision (signal-to-noise ratio, with values greater than 4.0 indicating adequate model discrimination), and the lack-of-fit test (with $p > 0.05$ indicating that the model adequately fits the data) [30]. All statistical tests were performed at a significance level of $\alpha = 0.05$.

**Table 3.** Variable Ranges used in RSM-BBD

| Variable | Unit | Symbol | Coded Variable Level | | |
|---|---|---|---|---|---|
| | | | Low | Center | High |
| | | | -1 | 0 | +1 |
| **ECH** | wt. % | A | 1.0 | 2.0 | 3.0 |
| **TCS** | wt. % | B | 0.3 | 1.0 | 1.7 |
| **SiO2** | wt. % | C | 0.5 | 2.0 | 3.5 |

* Corresponding to: R. A. Wahab (email: roswanira@utm.my)
DOI: https://doi.org/10.11113/jamst.v30n2.353

## 2.4 Membrane Characterization

### *2.4.1 Contact Angle Analysis*

The hydrophobicity of the fabricated membranes was evaluated by measuring water contact angles with a Krüss Easy Drop goniometer (Krüss GmbH, Germany) equipped with DSA100 software for image analysis and angle determination. Membrane samples measuring 5 mm × 15 mm were carefully cut and fixed onto glass slides (25 mm × 75 mm × 1 mm) using double-sided tape to prevent curling or movement during measurement. A sessile drop of 1 μL Milli-Q water was gently deposited onto the membrane surface using a precision syringe (Hamilton, 5 μL), and its shape was captured immediately (within 5 s of deposition) with a high-resolution camera to minimize evaporation. Contact angles were determined automatically using the Young–Laplace fitting method, which accounts for the drop profile and gravitational distortion [31].

To ensure statistical reliability, five measurements were performed at different locations on each of three independently prepared membranes for each experimental condition, yielding a total of 15 measurements per condition. The mean value and standard deviation were then calculated and reported. All measurements were conducted in a controlled environment at 25 ± 0.5 °C and 50 ± 5% relative humidity. Prior to measurement, the goniometer was calibrated using a standard calibration block of known contact angle, and the instrument was zeroed between each set of measurements.

### *2.4.2 Water Flux and Salt Rejection Testing*

Direct Contact Membrane Distillation (DCMD) experiments were conducted using a laboratory-scale in-house setup designed to evaluate the desalination performance of the fabricated membranes. The membrane module consisted of a stainless steel cross-flow cell with an effective membrane area of $2.827 \times 10^{-3}$ m² (diameter = $6.0 \times 10^{-2}$ m). The experimental setup comprised two circulating streams: a hot feed stream and a cold permeate stream. The hot feed stream, consisting of a 3.5 wt.% NaCl solution prepared in deionized water, was maintained at 80 °C using a thermoregulated pump (Protech Model 830-S2) providing temperature control within ±0.1 °C. The cold permeate stream, consisting of deionised water, was maintained at 10 °C using a chiller (S&A CW-5000) with temperature control within ±0.5 °C. Both streams were circulated at a flow rate of 1.2 L/min using peristaltic pumps (Masterflex L/S, Cole-Parmer, USA) [32].

Prior to data collection, the system was allowed to run for 1 h to achieve thermal and hydraulic steady-state conditions, with steady-state defined as a permeate flux variation of less than ±2% over a 30 min period [33]. Following equilibration, the permeate weight was continuously monitored over a 3 h period using an electronic balance (A3361 LT5001E Smith, ±0.01 g accuracy) connected to a data logging system, with weight readings recorded every 10 min. The permeate flux, $J_v$ (kg·m$^{-2}$·h$^{-1}$), was calculated using the equation:

$$J_v = \Delta W / A.\Delta_t \quad (2)$$

where $\Delta W$ is the mass of permeate collected (kg), $A$ is the effective membrane area (m²), and $\Delta t$ is the collection time (h). The salt rejection, $R$ *(%)*, was determined by measuring

* Corresponding to: R. A. Wahab (email: roswanira@utm.my)
DOI: https://doi.org/10.11113/jamst.v30n2.353

the electrical conductivity of the feed and permeate solutions using a calibrated conductivity meter (Hach HQ40d, Hach Company, USA) and calculated using the equation:

$$R(\%) = \frac{C_f - C_p}{C_f} \times 100 \quad (3)$$

where $C_f$ and $C_p$ are the NaCl concentrations (ppm) in the feed and permeate solutions, respectively. The conductivity meter was calibrated daily using standard NaCl solutions prepared over the concentration range of 0–50,000 ppm. All DCMD experiments were performed in triplicate using independently prepared membranes, and the results are reported as mean values with standard deviations.

### *2.4.3 Total Porosity Analysis*

The total porosity of the membranes was determined using the wet–dry gravimetric method, a widely accepted technique for assessing membrane porosity based on the weight difference between wet and dry states [34]. Membrane samples measuring 4 cm × 4 cm were cut from each membrane (n = 3 per condition) and immersed in deionized water at 25 °C for 24 h to ensure complete saturation of the pore structure. After the immersion period, the wet samples were removed, and surface water was gently blotted with tissue paper (Kimwipes, Kimberly-Clark) to remove excess moisture without removing water from within the pores. The wet weight ($W_{wet}$) was immediately recorded using an analytical balance with a precision of ±0.0001 g.

The samples were then dried in a vacuum oven (Memmert VO 200) at 60 °C under reduced pressure (100 mbar) for 48 h to ensure complete removal of water from the membrane pores. The dry weight ($W_{\mathrm{dry}}$) was measured after the samples were cooled in a desiccator to prevent moisture adsorption. Membrane thickness was measured at five randomly selected locations using a digital micrometer (Mitutoyo MDC-25S, ±0.001 mm precision), and the average thickness was used for porosity calculations [35]. The porosity was calculated using the following equation:

$$Porosity(\%) = \frac{W_{wet} - W_{dry}}{A \times d \times \rho_m} \times 100 \quad (4)$$

where $A$ is the membrane area (m²), $d$ is the membrane thickness (m), and $\rho_m$ is the density of water at 25 °C (1000 kg·m$^{-3}$).

### *2.4.4 ATR-FTIR Spectroscopy*

Attenuated Total Reflectance–Fourier Transform Infrared (ATR-FTIR) spectroscopy was employed to characterise the chemical composition and functional groups present in the fabricated membranes, thereby confirming the successful incorporation of the various components. Spectra were recorded using a PerkinElmer Spectrum 2000 spectrometer equipped with a diamond ATR crystal accessory (Specac Golden Gate, single-reflection configuration). Membrane samples measuring 5 mm × 5 mm were placed onto the diamond crystal and pressed firmly using the integrated anvil mechanism to ensure intimate contact

* Corresponding to: R. A. Wahab (email: roswanira@utm.my)
DOI: https://doi.org/10.11113/jamst.v30n2.353

between the sample and the crystal surface. A background spectrum was collected prior to each sample measurement using the clean, dry crystal surface as the reference. Spectra were acquired over the wavenumber range of 600–4000 $cm^{-1}$, with each spectrum averaged from 32 scans at a resolution of 4 $cm^{-1}$ to improve signal-to-noise ratio. The background spectrum was automatically subtracted from each sample spectrum using the Perkin-Elmer software (Alizadeh *et al*., 2019). All measurements were performed in triplicate on different areas of each membrane sample to ensure reproducibility. The ATR crystal was cleaned with ethanol and dried between samples to prevent cross-contamination. Peak identification and assignment were performed by comparison with reference spectra from the literature and the NIST Chemistry WebBook database.

### *2.4.5 Scanning Electron Microscopy*

The surface morphology and cross-sectional structure of the membranes were examined using a Hitachi TM3000 Tabletop Scanning Electron Microscope (Hitachi High-Technologies, Japan) operated at an accelerating voltage of 10 kV. For cross-sectional observation, membrane samples (5 mm × 5 mm) were immersed in liquid nitrogen for 15 s to embrittle the polymer, after which they were fractured using tweezers to obtain a clean, brittle fracture surface that revealed the internal pore structure without introducing deformation artefacts. Both surface and cross-section samples were mounted onto aluminum stubs using conductive carbon tape. To prevent charging effects during electron-beam irradiation, the samples were sputter-coated with platinum using a Quorum Q150R ES sputter coater at 15 mA for 120 s, yielding a coating thickness of approximately 5–10 nm. Coated samples were stored in a desiccator and examined within 24 h of preparation.

Images were acquired at magnifications of 2.0k, 5.0k, and 10.0k to capture both the overall membrane architecture and the fine surface details. For quantitative pore-size analysis, the acquired SEM images were processed using ImageJ (NIH, version 1.53t). The images were calibrated using the SEM scale bar, and regions of interest were selected from representative areas of each image. A minimum of 50 pores were measured per image using the Feret diameter method, which determines the longest distance between two parallel lines tangent to the pore boundary. Pore size distributions were constructed and mean pore diameters calculated for each membrane condition.

## 2.5 Statistical Analysis and Data Reporting

All experimental data are expressed as mean ± standard deviation (SD) calculated from triplicate independent experiments. Statistical analyses were performed using Design-Expert software (Version 13.0.5.0, Stat-Ease Inc., USA). Analysis of variance (ANOVA) was used to assess the significance of the model and its individual terms, with p-values $< 0.05$ considered statistically significant. Graphical representations, including three-dimensional surface and contour plots, were generated using the same software to visualize interactions among factors and their effects on the response variables. Multi-response optimization was performed using the desirability function approach to simultaneously maximize contact angle, water flux, and salt rejection. The formulation with the highest overall desirability was selected as the optimal condition.

* Corresponding to: R. A. Wahab (email: roswanira@utm.my)
DOI: https://doi.org/10.11113/jamst.v30n2.353

## 3.0 RESULTS AND DISCUSSION

### 3.1 Membrane Formation and Fabrication

The MWCNT/$SiO_2$/ECH/TCS-PVDF membrane was successfully fabricated using the phase inversion method, followed by surface modification with triclosan (TCS). This approach has been widely adopted for preparing porous polymeric membranes with controllable morphology and high reproducibility [13, 27]. The phase inversion process involves the controlled precipitation of a polymer solution in a non-solvent bath, yielding a porous structure via liquid-liquid demixing [41]. In this study, the incorporation of LiCl and PEG as pore-forming agents facilitated the formation of interconnected pore structures, which are essential for achieving high water flux [41]. Visual inspection of the resulting membranes revealed a grey appearance across all formulations, with the top surface darker than the bottom (Figure 1ai-ii).

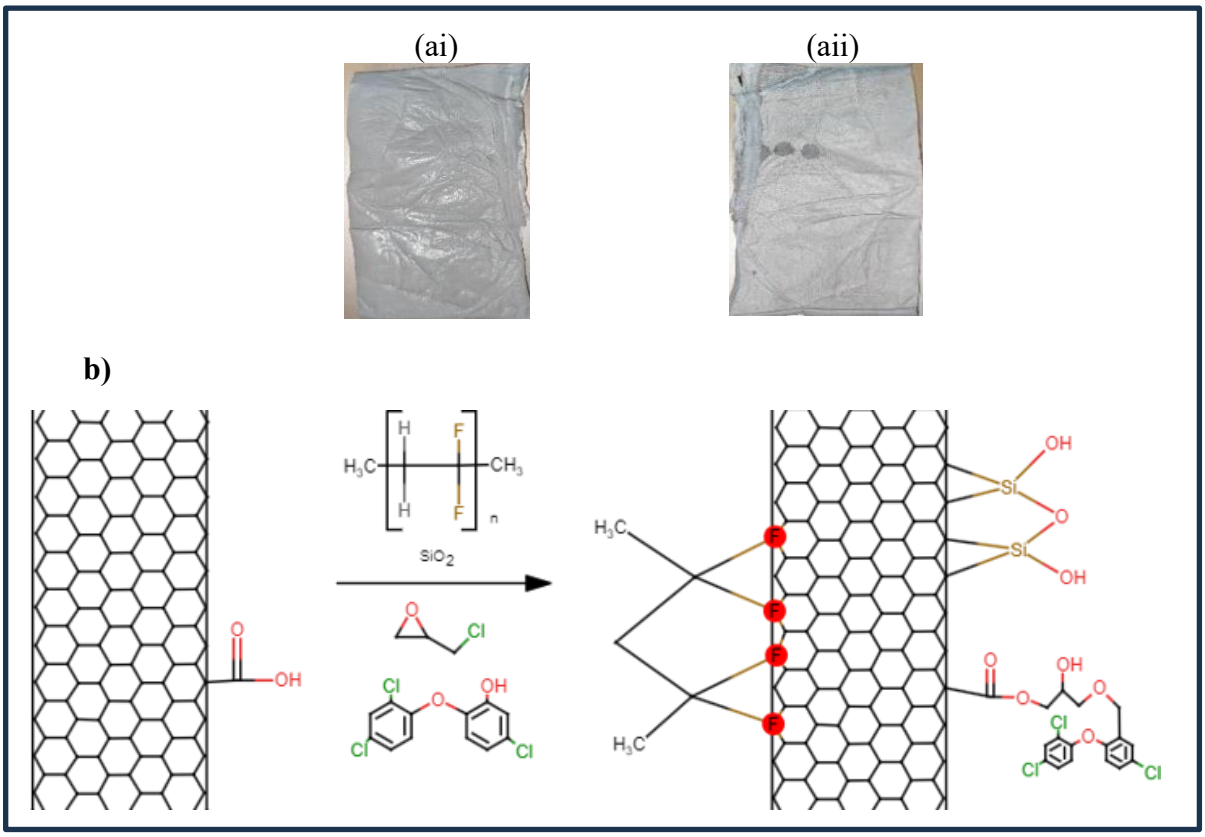


**Figure 1.** (a) MWCNT/$SiO_2$/ECH/TCS-PVDF membrane: (ai) top view and (aii) bottom view; (b) schematic diagram of the MWCNT/$SiO_2$/ECH/TCS-PVDF membrane preparation

This color gradient is attributed to the differential distribution of MWCNTs during the phase inversion process, in which the top surface, in direct contact with the coagulation bath, undergoes faster solvent exchange, leading to more concentrated nanoparticle deposition near the surface [18]. The darker top surface is characteristic of membranes

* Corresponding to: R. A. Wahab (email: roswanira@utm.my)
DOI: https://doi.org/10.11113/jamst.v30n2.353

containing carbon-based nanomaterials, as MWCNTs impart a dark coloration due to their high carbon content and light-absorbing properties [16]. The schematic representation of the membrane preparation (Figure 1b) illustrates the chemical transformations involved in forming the MWCNT/$SiO_2$/ECH/TCS-PVDF membrane. The process begins with the reaction between the carboxylic acid groups on the functionalized MWCNT (MWCNT-COOH) and the epoxide ring of epichlorohydrin (ECH). While ECH does not readily form ester bonds with carboxylic acids under normal conditions, the C=O ester peak observed in the FTIR spectra (1733.04 $cm^{-1}$) confirms the presence of ester functionalities originating from the MWCNT-COOH starting material [24]. The phenolic hydroxyl group of TCS subsequently acts as a nucleophile, attacking the epoxide ring to form a covalent ether linkage, yielding MWCNT-ECH-TCS [21]. The C=O ester peak observed at 1733.04 $cm^{-1}$ in the FTIR spectra is attributed to residual carboxylic acid groups on the MWCNT-COOH starting material. The $SiO_2$ particles are incorporated into the membrane to enhance the mechanical properties and stability of the composite membrane, likely through physical adsorption or hydrogen bonding facilitated by surface hydroxyl groups on the $SiO_2$ [19]. The $SiO_2$ particles are incorporated to enhance the mechanical properties and stability of the composite membrane, likely through physical adsorption or covalent bonding facilitated by surface hydroxyl groups on the $SiO_2$ [19]. The functionalized MWCNTs and $SiO_2$ are then dispersed in the PVDF matrix, forming the final composite membrane.

## 3.2 Optimization Using Response Surface Methodology (RSM)

The membrane formulation was optimized using the Box–Behnken Design (BBD) within the Response Surface Methodology framework. This approach is particularly well-suited for identifying optimal conditions with fewer experimental runs, making it both efficient and cost-effective for multi-component membrane fabrication studies [25, 26]. The experimental design consisted of three factors: ECH concentration (1.0–3.0 wt.%), TCS concentration (0.3–1.7 wt.%), and $SiO_2$ concentration (0.5–3.5 wt.%). The following subsections report the evaluated responses: contact angle, water flux, and salt rejection.

### *3.2.1 Contact Angle*

The contact angle response provides a direct measure of membrane hydrophobicity, which is crucial for preventing pore wetting in membrane distillation applications [8]. Higher contact angles indicate greater hydrophobicity, which is desirable for maintaining a stable vapor-liquid interface and preventing liquid penetration into the membrane pores. While superhydrophobic membranes (>150°) represent the ideal for MD applications, the contact angles achieved in this study (70–93°) indicate hydrophobic behavior, which may be sufficient for moderate MD performance but requires further optimization for robust wetting resistance [7, 15]. Higher contact angles indicate greater hydrophobicity, which is desirable for maintaining a stable vapor-liquid interface and preventing liquid penetration into the membrane pores. The ANOVA results for the quadratic model fitted to the contact angle data are presented in Table 4.

* Corresponding to: R. A. Wahab (email: roswanira@utm.my)
DOI: https://doi.org/10.11113/jamst.v30n2.353

**Table 4.** ANOVA for Quadratic Model for Contact Angle Response

| Source | Sum of Squares | df | Mean Square | F-value | p-value | |
|---|---|---|---|---|---|---|
| **Model** | 647.51 | 9 | 71.95 | 1.26 | 0.3869 | not significant |
| A-ECH | 1.57 | 1 | 1.57 | 0.0275 | 0.8729 | |
| B-TCS | 30.69 | 1 | 30.69 | 0.5396 | 0.4865 | |
| C-SiO2 | 303.93 | 1 | 303.93 | 5.34 | 0.0541 | |
| AB | 61.94 | 1 | 61.94 | 1.09 | 0.3314 | |
| AC | 17.06 | 1 | 17.06 | 0.2999 | 0.6010 | |
| BC | 127.58 | 1 | 127.58 | 2.24 | 0.1779 | |
| $A^2$ | 20.07 | 1 | 20.07 | 0.3528 | 0.5712 | |
| $B^2$ | 2.06 | 1 | 2.06 | 0.0362 | 0.8545 | |
| $C^2$ | 79.70 | 1 | 79.70 | 1.40 | 0.2752 | |
| **Residual** | 398.15 | 7 | 56.88 | | | |
| Lack of Fit | 90.83 | 3 | 30.28 | 0.3941 | 0.7649 | not significant |
| Pure Error | 307.32 | 4 | 76.83 | | | |
| **Cor Total** | 1045.67 | 16 | | | | |

The overall model had a p-value of 0.3869, indicating it was not statistically significant ($p > 0.05$). This suggests that the model does not adequately explain the variability in the contact angle response within the experimental domain examined. Among the individual factors, $SiO_2$ (Factor C) showed marginal significance ($p = 0.0541$), suggesting that $SiO_2$ concentration may have a more pronounced effect on hydrophobicity compared to ECH and TCS. The lack of significance for ECH ($p = 0.8729$) and TCS ($p = 0.4865$) indicates that variations in these factors did not substantially affect the contact angle within the tested ranges. This observation is consistent with findings from Zhang *et al*. [15], who reported that $SiO_2$ nanoparticles significantly enhanced the hydrophobicity of PVDF membranes by increasing surface roughness, whereas the effect of organic modifiers was less pronounced.

The fit statistics (Table 5a) showed that the contact angle model had low explanatory power ($R^2 = 0.6192$, adjusted $R^2 = 0.1297$) and poor predictive capability (predicted $R^2 = -0.8491$), indicating that the model is not robust for prediction despite an adequate signal-to-noise ratio (Adeq Precision = 4.2250). Thus, this value indicates a modest signal-to-noise ratio, just adequate for model discrimination [30]. The lack-of-fit test was not significant ($p = 0.7649$), confirming adequate model fit to the existing data [30]. The coefficients for coded factors (Table 5b) revealed that none of the individual factors or interaction terms were statistically significant ($p > 0.05$), suggesting that the selected factor ranges did not adequately capture the variability in contact angle. Further refinement of the model with a wider range of conditions may be necessary to improve its predictive capability [56].

Despite the limited predictive capability of the contact angle model, the optimization and selection of Run 17 as the optimal condition was based on a multi-response desirability function approach that simultaneously considered all three performance metrics (contact angle, salt rejection, and water flux). This approach allowed identification of the

* Corresponding to: R. A. Wahab (email: roswanira@utm.my)
DOI: https://doi.org/10.11113/jamst.v30n2.353

formulation that provided the best overall compromise among the three responses, even though individual models showed varying degrees of statistical significance. The salt rejection model (Table 6) and water flux model (Table 8) exhibited better statistical performance, justifying the use of multi-response optimization. The adequate precision value of 4.2250 indicates a modest signal-to-noise ratio, just adequate for model discrimination [30]. Hence, the findings of this study suggest that while the model may describe the observed data, it is not robust for prediction. Further refinement of the model, potentially by including additional factors or exploring a wider range of conditions, may be necessary to improve its predictive capability [56].

**Table 5.** a) The Fit Statistic for the Quadratic Model and b) Coefficients in Terms of Coded Factors for Contact Angle

a)

| | | | |
|---|---|---|---|
| **Std. Dev.** | 7.54 | $R^2$ | 0.6192 |
| **Mean** | 82.14 | Adjusted $R^2$ | 0.1297 |
| **C.V. %** | 9.18 | Predicted $R^2$ | -0.8491 |
| | | Adeq Precision | 4.2250 |

b)

| Factor | Coefficient Estimate | df | Standard Error | 95% CI Low | 95% CI High | VIF |
|---|---|---|---|---|---|---|
| Intercept | 84.88 | 1 | 3.37 | 76.91 | 92.86 | |
| A-ECH | 0.4425 | 1 | 2.67 | -5.86 | 6.75 | 1.0000 |
| B-TCS | -1.96 | 1 | 2.67 | -8.26 | 4.35 | 1.0000 |
| C-SiO2 | 6.16 | 1 | 2.67 | -0.1414 | 12.47 | 1.0000 |
| AB | 3.94 | 1 | 3.77 | -4.98 | 12.85 | 1.0000 |
| AC | 2.07 | 1 | 3.77 | -6.85 | 10.98 | 1.0000 |
| BC | -5.65 | 1 | 3.77 | -14.56 | 3.27 | 1.0000 |
| $A^2$ | -2.18 | 1 | 3.68 | -10.87 | 6.51 | 1.01 |
| $B^2$ | 0.6993 | 1 | 3.68 | -7.99 | 9.39 | 1.01 |
| $C^2$ | -4.35 | 1 | 3.68 | -13.04 | 4.34 | 1.01 |

### *3.2.2 Salt Rejection*

The salt rejection response is a critical performance metric for desalination membranes, representing the membrane's ability to retain NaCl while allowing water vapor to pass through [40]. The ANOVA results for the reduced cubic model fitted to the salt rejection data are presented in Table 6. The model exhibited a significant p-value of 0.0346, indicating that the reduced cubic model was statistically significant and explained a meaningful portion of the variability in salt rejection. Among the individual factors, $SiO_2$ (Factor C) showed marginal significance ($p = 0.0652$), while TCS (Factor B) was not significant ($p = 0.3877$). This suggests that $SiO_2$ may play a more important role in determining salt rejection, likely due to its influence on membrane surface morphology and porosity [39]. The quadratic term of $SiO_2$ ($C^2$) was significant ($p = 0.0214$), indicating a non-linear relationship between $SiO_2$ concentration and salt rejection. The interaction term $BC^2$ (between TCS and the squared term of $SiO_2$) was also significant ($p = 0.0395$), suggesting a complex interplay between these factors in influencing salt rejection.

* Corresponding to: R. A. Wahab (email: roswanira@utm.my)
DOI: https://doi.org/10.11113/jamst.v30n2.353

**Table 6.** ANOVA for Reduced Cubic Model for Salt Rejection

| Source | Sum of Squares | df | Mean Square | F-value | p-value | |
|---|---|---|---|---|---|---|
| **Model** | 741.19 | 5 | 148.24 | 3.64 | 0.0346 | significant |
| B-TCS | 32.95 | 1 | 32.95 | 0.8090 | 0.3877 | |
| C-$SiO_2$ | 170.85 | 1 | 170.85 | 4.19 | 0.0652 | |
| BC | 9.77 | 1 | 9.77 | 0.2398 | 0.6340 | |
| $C^2$ | 292.46 | 1 | 292.46 | 7.18 | 0.0214 | |
| $BC^2$ | 222.08 | 1 | 222.08 | 5.45 | 0.0395 | |
| **Residual** | 447.99 | 11 | 40.73 | | | |
| Lack of Fit | 130.84 | 7 | 18.69 | 0.2357 | 0.9532 | not significant |
| Pure Error | 317.15 | 4 | 79.29 | | | |
| **Cor Total** | 1189.18 | 16 | | | | |

The salt rejection model showed moderate explanatory power ($R^2 = 0.6233$, adjusted $R^2 = 0.4520$) and an adequate signal-to-noise ratio (Adeq Precision = 6.6022), though the low predicted $R^2$ (0.1163) suggests some overfitting (Table 7a) [30]. Coefficient estimates (Table 7b) indicated that TCS negatively impacted salt rejection (coefficient = -2.87), possibly due to pore blockage or defect introduction [23], while $SiO_2$ had a positive effect (coefficient = 4.62), likely through improved membrane structure and hydrophobicity [15].

**Table 7**. a) Fit Statistic for Reduced Cubic Model and b) Coefficients in Terms of Coded Factors for Salt Rejection

**a)**

| | | | | |
|---|---|---|---|---|
| **Std. Dev.** | 6.38 | | **$R^2$** | 0.6233 |
| **Mean** | 59.73 | | **Adjusted $R^2$** | 0.4520 |
| **C.V. %** | 10.68 | | **Predicted $R^2$** | 0.1163 |
| | | | **Adeq Precision** | 6.6022 |

**b)**

| Factor | Coefficient Estimate | df | Standard Error | 95% CI Low | 95% CI High | VIF |
|---|---|---|---|---|---|---|
| Intercept | 63.64 | 1 | 2.13 | 58.96 | 68.32 | |
| B-TCS | -2.87 | 1 | 3.19 | -9.89 | 4.15 | 2.00 |
| C-SiO2 | 4.62 | 1 | 2.26 | -0.3448 | 9.59 | 1.0000 |
| BC | -1.56 | 1 | 3.19 | -8.59 | 5.46 | 1.0000 |
| $C^2$ | -8.31 | 1 | 3.10 | -15.14 | -1.48 | 1.0000 |
| $BC^2$ | 10.54 | 1 | 4.51 | 0.6054 | 20.47 | 2.00 |

### *3.2.3 Water Flux*

Water flux is a key performance indicator for membrane distillation, representing the rate of water vapor permeation through the membrane [33]. The ANOVA results for the linear model fitted to the water flux data are presented in Table 8. The overall model was not significant (p = 0.1463), indicating that the linear model does not adequately explain

* Corresponding to: R. A. Wahab (email: roswanira@utm.my)
DOI: https://doi.org/10.11113/jamst.v30n2.353

the variability in water flux. Among the individual factors, only $SiO_2$ (Factor C) was significant (p = 0.0352), while ECH (p = 0.3866) and TCS (p = 0.8230) were not significant. This indicates that $SiO_2$ concentration is the primary factor influencing water flux within the tested ranges. The lack-of-fit test yielded a p-value of 0.9557, confirming that the model does not have systematic deviation from the actual data patterns. The water flux model exhibited limited explanatory power ($R^2$ = 0.3291, adjusted $R^2$ = 0.1743) and poor predictive capability (predicted $R^2$ = 0.0127), despite an adequate signal-to-noise ratio (Adeq Precision = 4.7316) (Table 9a) [30]. Coefficient estimates (Table 9b) indicated that $SiO_2$ positively influenced flux (coefficient = 1.18, p = 0.0352), likely through enhanced porosity, while ECH and TCS showed negative but non-significant effects (coefficients = -0.4512 and -0.1150, respectively) [40].

**Table 8.** ANOVA for Reduced Cubic Model for Water Flux

| Source | Sum of Squares | df | Mean Square | F-value | p-value | |
|---|---|---|---|---|---|---|
| **Model** | 12.94 | 3 | 4.31 | 2.13 | 0.1463 | not significant |
| A-ECH | 1.63 | 1 | 1.63 | 0.8025 | 0.3866 | |
| B-TCS | 0.1058 | 1 | 0.1058 | 0.0521 | 0.8230 | |
| C-$SiO_2$ | 11.21 | 1 | 11.21 | 5.52 | 0.0352 | |
| **Residual** | 26.39 | 13 | 2.03 | | | |
| Lack of Fit | 9.80 | 9 | 1.09 | 0.2624 | 0.9557 | not significant |
| Pure Error | 16.59 | 4 | 4.15 | | | |
| **Cor Total** | 39.33 | 16 | | | | |

**Table 9.** a) Fit Statistic for Reduced Cubic Model and b) Coefficients in Terms of Coded Factors for Water Flux

**a)**

| | | | |
|---|---|---|---|
| **Std. Dev.** | 1.42 | **$R^2$** | 0.3291 |
| **Mean** | 10.06 | **Adjusted $R^2$** | 0.1743 |
| **C.V. %** | 14.16 | **Predicted $R^2$** | 0.0127 |
| | | **Adeq Precision** | 4.7316 |

**b)**

| Factor | Coefficient Estimate | df | Standard Error | 95% CI Low | 95% CI High | VIF |
|---|---|---|---|---|---|---|
| Intercept | 10.06 | 1 | 0.3455 | 9.32 | 10.81 | |
| A-ECH | -0.4512 | 1 | 0.5037 | -1.54 | 0.6370 | 1.0000 |
| B-TCS | -0.1150 | 1 | 0.5037 | -1.20 | 0.9732 | 1.0000 |
| C-SiO2 | 1.18 | 1 | 0.5037 | 0.0955 | 2.27 | 1.0000 |

### 3.3 Interactive Effect of Factors

The 3D surface plots provide valuable insights into the interactive effects of the factors on the responses. For salt rejection (Figure 2a), the curvature and varying gradients

* Corresponding to: R. A. Wahab (email: roswanira@utm.my)
DOI: https://doi.org/10.11113/jamst.v30n2.353

in the plot indicate a significant interaction between TCS and $SiO_2$ concentrations. The significant interaction term ($BC^2$) in the model further supports this observation. This interaction suggests that the effect of TCS on salt rejection depends on the $SiO_2$ concentration, and vice versa. At higher $SiO_2$ concentrations, the negative impact of TCS on salt rejection may be mitigated, likely due to the dominant effect of $SiO_2$ in enhancing membrane structure and hydrophobicity [57].

For the contact angle (Figure 2b), the surface plot illustrates the interaction between ECH and TCS, with notable curvature suggesting non-linear interactions. The response surface shows that contact angle tends to increase at intermediate levels of both ECH and TCS, while extreme values of either factor lead to reduced hydrophobicity. This observation is consistent with the findings of Guo *et al*. [24], who reported that excessive cross-linking with ECH can lead to membrane densification and reduced surface roughness, thereby decreasing hydrophobicity.

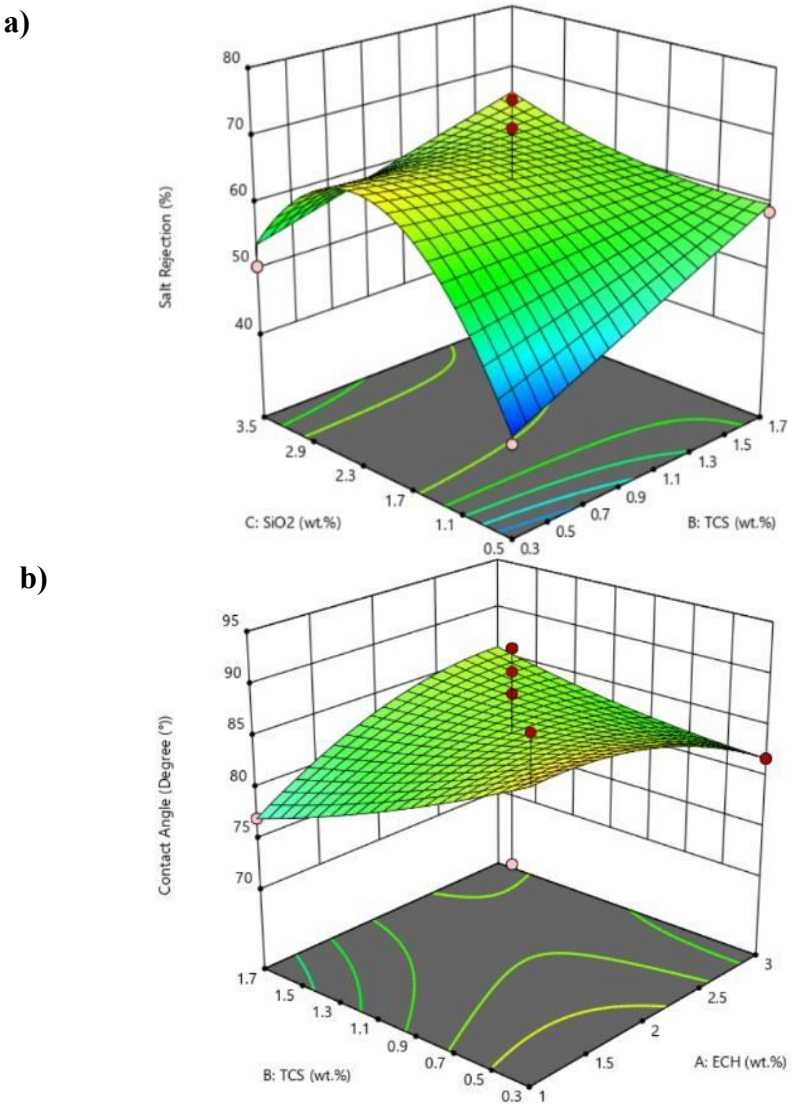


**Figure 2.** The 3D Surface Graph for Reduced Cubic Model for Salt Rejection and b) the Quadratic Model for Contact Angle

* Corresponding to: R. A. Wahab (email: roswanira@utm.my)
DOI: https://doi.org/10.11113/jamst.v30n2.353

### 3.4 Optimisation and Model Validation

The optimization was performed using the desirability function approach in Design-Expert software, with the objective of simultaneously maximizing all three responses: contact angle (goal: maximize to ≥150°), water flux (goal: maximize to ≥10 $kg \cdot m^{-2} \cdot h^{-1}$), and salt rejection (goal: maximize to ≥95%). Equal weighting (importance = 3) was assigned to each response to avoid bias toward any single performance metric. The optimization results from the Box–Behnken Design (Table 10) identified Run 17 as the optimal condition, with factor levels of 2 wt.% ECH, 1 wt.% TCS, and 2 wt.% $SiO_2$. This condition yielded a contact angle of 92.98°, a water flux of 11.05 $kg \cdot m^{-2} \cdot h^{-1}$, and a salt rejection rate of 75.36 %. It should be noted that while the contact angle model alone showed limited statistical significance (Table 4), the selection of Run 17 was based on a multi-response optimization approach that simultaneously maximized all three performance metrics. The desirability function in Design-Expert software identified this formulation as the best compromise, with the salt rejection and water flux models providing stronger statistical support for this selection. These findings indicate moderate hydrophobicity, good flux performance, and substantial salt rejection capability.

The salt rejection rate achieved in this study (75.36%) is substantially lower than the near-complete (>99%) rejection reported for some superhydrophobic PVDF membranes [58, 7]. For instance, Teoh *et al*. [56] demonstrated that superhydrophobic PVDF membranes with hierarchical surface structures maintained 99.9% salt rejection over extended DCMD operation. Similarly, Pan *et al*. [57] reported that PVDF membranes with 3D flower-like LDH structures achieved stable salt rejection during MD desalination of hypersaline water. The lower rejection observed in this study can be attributed to several factors. First, the moderate contact angle (92.98°) achieved is well below the superhydrophobic threshold of 150° [15]. Superhydrophobic membranes maintain a stable Cassie-Baxter state with trapped air pockets that minimize liquid-membrane contact, effectively preventing pore wetting [38]. The moderate hydrophobicity of the current membrane likely allows partial penetration of liquid into the pores, compromising salt rejection [40]. Second, the presence of undissolved TCS crystals observed in SEM images (Figure 6f) may create localized surface defects that serve as initiation sites for pore wetting [23]. Third, the trade-off between flux and salt rejection is well documented in the membrane distillation literature; increasing porosity to enhance flux can reduce salt rejection if pore size exceeds the critical threshold for liquid entry pressure [9]. Despite these limitations, the achieved flux (11.05 $kg \cdot m^{-2} \cdot h^{-1}$) is encouraging and exceeds the 10 $kg \cdot m^{-2} \cdot h^{-1}$ benchmark reported for practical DCMD applications [33]. This suggests that the membrane structure facilitates efficient water vapor transport, and that further optimization of surface chemistry and morphology could significantly improve salt rejection.

The lower rejection observed in this study (75.36%) can be attributed to several interconnected factors; firstly, the moderate contact angle (92.98°) is well below the superhydrophobic threshold of 150° [15]. Superhydrophobic membranes maintain a stable Cassie-Baxter state with trapped air pockets that minimize liquid-membrane contact, effectively preventing pore wetting [38]. At contact angles below 150°, the transition from Cassie-Baxter to Wenzel state becomes more likely, allowing partial liquid penetration into pores and compromising salt rejection [40]. Second, the presence of undissolved TCS

* Corresponding to: R. A. Wahab (email: roswanira@utm.my)
DOI: https://doi.org/10.11113/jamst.v30n2.353

crystals observed on the membrane surface (Figure 5f) likely creates localized defects that serve as initiation sites for pore wetting [23]. These crystals disrupt the uniform hydrophobic surface, creating pathways for liquid penetration. Third, the non-uniform pore size distribution observed in SEM images (Figure 5d-f), with pores ranging from 133 nm to 219 nm, may contribute to performance variability. Regions with larger pores are more susceptible to wetting, as the liquid entry pressure decreases with increasing pore size [50]. Finally, the trade-off between flux and salt rejection is well documented in the MD literature [9]. The high porosity (82.40%) achieved in this study, while beneficial for flux, may increase the risk of pore wetting if pore sizes exceed the critical threshold for liquid entry pressure [33].

Collectively, these factors explain the moderate salt rejection and highlight the need for improved surface modification strategies, including more uniform TCS deposition, hierarchical surface structuring for superhydrophobicity, and tighter pore size control, in order to achieve the >99% rejection required for practical DCMD applications.

**Table 10.** Factors and Response Data for the Box-Behnken Optimization for producing the PVDF-MWCNT-Triclosan Hybrid Membrane

| Run | Factor 1 A: ECH (wt.%) | Factor 2 B: TCS (wt.%) | Factor 3 C: SiO2 (wt.%) | Response 1 Contact Angle (°) | Response 2 Salt Rejection (%) | Response 3 Water Flux (kg $m^{-2}$ $hr^{-1}$) |
|---|---|---|---|---|---|---|
| **1** | 3 | 0.3 | 2.0 | 81.87 | 60.25 | 10.64 |
| **2** | 2 | 0.3 | 3.5 | 91.74 | 50.46 | 10.97 |
| **3** | 1 | 1.0 | 3.5 | 80.71 | 63.23 | 11.78 |
| **4** | 2 | 1.0 | 2.0 | 71.83 | 55.05 | 9.34 |
| **5** | 2 | 1.0 | 2.0 | 90.77 | 71.25 | 12.38 |
| **6** | 2 | 1.7 | 3.5 | 81.09 | 62.67 | 12.02 |
| **7** | 2 | 0.3 | 0.5 | 70.08 | 40.3 | 8.26 |
| **8** | 2 | 1.7 | 0.5 | 82.02 | 58.76 | 10.05 |
| **9** | 2 | 1.0 | 2.0 | 80.16 | 60.75 | 9.06 |
| **10** | 1 | 0.3 | 2.0 | 93.41 | 72.02 | 12.2 |
| **11** | 3 | 1.0 | 3.5 | 90.28 | 63.45 | 10.1 |
| **12** | 3 | 1.0 | 0.5 | 71.86 | 53.08 | 9.04 |
| **13** | 1 | 1.0 | 0.5 | 70.55 | 50.7 | 8.05 |
| **14** | 2 | 1.0 | 2.0 | 88.68 | 57.3 | 7.04 |
| **15** | 1 | 1.7 | 2.0 | 77.06 | 62.16 | 10.22 |
| **16** | 3 | 1.7 | 2.0 | 81.26 | 58.63 | 8.86 |
| **17** | 2 | 1.0 | 2.0 | 92.98 | 75.36 | 11.05 |

The novelty and practical significance of this work lie not in achieving benchmark performance but in several other contributions. First, this study demonstrates the successful covalent integration of TCS into MWCNT-ECH-functionalized PVDF membranes, as confirmed by ATR-FTIR analysis (Figures 4a-b), thereby creating a dual-functional system that combines enhanced hydrophobicity with antibacterial potential. This integration has not been previously reported for DCMD applications. Second, the systematic statistical

* Corresponding to: R. A. Wahab (email: roswanira@utm.my)
DOI: https://doi.org/10.11113/jamst.v30n2.353

optimization using RSM-BBD (Table 3) provides a robust framework for understanding the interactions among ECH, TCS, and $SiO_2$ concentrations and their effects on membrane performance. The identification of $SiO_2$ as the most influential factor ($p = 0.0352$ for flux, $p = 0.0541$ for contact angle) provides valuable guidance for future optimization efforts. Third, the 82.40% total porosity (Section 3.7) demonstrates this formulation's potential for high flux, and the reduction in pore size from 432–476 nm to 133–219 nm upon TCS coating (Section 3.9) confirms the feasibility of controlling pore architecture to improve salt rejection.

While the current salt rejection and contact angle do not meet industrial benchmarks, the trends observed in this study, particularly the enhancement of hydrophobicity upon TCS coating for certain formulations (Table 11) and the significant increase in porosity, appear to provide a solid foundation for future work. With improved TCS dispersion strategies (e.g., cosolvent use, ultrasonication) and optimization of surface roughness (e.g., hierarchical structuring), the current formulation could be further developed to achieve superhydrophobicity and >99% salt rejection.

### 3.5 Analysis of Contact Angle

The contact angle measurements before and after TCS coating provide insights into the effect of TCS on membrane hydrophobicity (Table 11). The most significant improvements were observed in Membrane 5, with an increase from 75.14° to 90.77° ($\Delta$ = 15.63°), and in Membrane 17, with an increase from 82.20° to 92.98° ($\Delta$ = 10.78°). These improvements suggest that TCS coating can enhance membrane hydrophobicity, likely due to the formation of a hydrophobic TCS layer on the membrane surface. TCS, with its phenolic hydroxyl and chlorinated aromatic groups, is known to reduce surface energy, thereby increasing contact angle [43]. This observation is consistent with the findings of Park *et al*. [23], who reported that TCS-immobilized polyamide membranes exhibited enhanced hydrophobicity and improved anti-biofouling properties.

However, some membranes exhibited a decrease in contact angle after TCS coating. For example, Membrane 7 decreased from 87.05° to 70.08° ($\Delta$ = -16.97°), and Membrane 13 decreased from 90.90° to 70.55° ($\Delta$ = -20.35°). These decreases suggest that TCS coating may not uniformly enhance hydrophobicity across all membrane types, possibly due to variations in the interaction between TCS and the membrane surface. Incomplete dissolution of TCS during the coating process, as evidenced by white crystals in SEM images (Figure 6f), may have contributed to these inconsistencies. The non-uniform deposition of TCS could lead to localized areas of reduced hydrophobicity, adversely affecting the overall contact angle [22]. Despite improvements observed in some membranes, none achieved superhydrophobicity (>150°). The highest contact angle recorded was 93.41° (Membrane 10), which falls considerably short of the superhydrophobic threshold. Achieving superhydrophobicity typically requires a combination of micro- and nanoscale surface roughness and chemical modifications that significantly reduce surface energy [15, 55]. The moderate contact angles observed in this study suggest that further optimisation of surface roughness and strategies for reducing surface energy are necessary. Future work should consider using hierarchical surface structures or incorporating additional hydrophobic nanoparticles to achieve superhydrophobicity [45].

* Corresponding to: R. A. Wahab (email: roswanira@utm.my)
DOI: https://doi.org/10.11113/jamst.v30n2.353

**Table 11.** Contact angle measurements before and after TCS coating for the MWCNT/$SiO_2$/ECH/TCS-PVDF membrane

| Membrane | Contact Angle Before TCS Coating (°) | Contact Angle After TCS Coating (°) | Change in Contact Angle (°) |
|---|---|---|---|
| **1** | 81.91 | 81.87 | -0.04 |
| **2** | 84.71 | 91.74 | +7.03 |
| **3** | 79.01 | 80.71 | +1.70 |
| **4** | 84.71 | 71.83 | -12.88 |
| **5** | 75.14 | 90.77 | +15.63 |
| **6** | 74.96 | 81.09 | +6.13 |
| **7** | 87.05 | 70.08 | -16.97 |
| **8** | 88.99 | 82.02 | -6.97 |
| **9** | 71.02 | 80.16 | +9.14 |
| **10** | 93.01 | 93.41 | +0.40 |
| **11** | 83.26 | 90.28 | +7.02 |
| **12** | 83.26 | 71.86 | -11.40 |
| **13** | 90.90 | 70.55 | -20.35 |
| **14** | 91.56 | 88.68 | -2.88 |
| **15** | 89.36 | 77.06 | -12.30 |
| **16** | 79.17 | 81.26 | +2.09 |
| **17** | 82.20 | 92.98 | +10.78 |

### 3.6 Analysis on Flux and Salt Rejection

The flux and salt rejection data for the 17 experimental runs are presented in Table 12. The flux values ranged from 7.04 to 12.38 $kg \cdot m^{-2} \cdot h^{-1}$, with several membranes exceeding the benchmark of 10 $kg \cdot m^{-2} \cdot h^{-1}$. Membrane 5 exhibited the highest flux (12.38 $kg \cdot m^{-2} \cdot h^{-1}$), followed by Membranes 10 (12.20 $kg \cdot m^{-2} \cdot h^{-1}$) and 6 (12.02 $kg \cdot m^{-2} \cdot h^{-1}$). The optimal membrane (Run 17) achieved a flux of 11.05 $kg \cdot m^{-2} \cdot h^{-1}$, surpassing the benchmark. The flux achieved in this study is comparable to the 9.6–15.3 $L \cdot m^{-2} \cdot h^{-1}$ reported for PVDF membranes with various nano-additives [17], and higher than the 8.8–10.3 $kg \cdot m^{-2} \cdot h^{-1}$ reported for pure PVDF membranes operated under similar DCMD conditions [51]. This indicates that incorporating MWCNT, $SiO_2$, and TCS enhances flux, likely through increased porosity and improved surface structure [19].

Salt rejection values varied considerably, ranging from 40.30% to 75.36%. The highest salt rejection was observed in Membrane 17 (75.36%), followed by Membranes 10 (72.02%) and 5 (71.25%). However, none of the membranes met the target benchmark of 95–99% salt rejection. This is significantly lower than the near-complete salt rejection (>99 %) reported for superhydrophobic membranes [58, 7]. The moderate salt rejection in this study may be attributed to the membranes' moderate hydrophobicity, which may allow some liquid water to penetrate the pores, thereby reducing rejection [40]. Additionally, the presence of undissolved

* Corresponding to: R. A. Wahab (email: roswanira@utm.my)
DOI: https://doi.org/10.11113/jamst.v30n2.353

TCS crystals on the membrane surface, as observed in SEM images, may create localized defects that compromise salt-rejection capability [23].

**Table 12.** The flux and salt rejection data for the 17 experimental runs

| Membrane | Flux (kg·m−2·h−1) | Salt Rejection (%) |
|---|---|---|
| **1** | 10.64 | 60.25 |
| **2** | 10.97 | 50.46 |
| **3** | 11.78 | 63.23 |
| **4** | 9.34 | 55.05 |
| **5** | 12.38 | 71.25 |
| **6** | 12.02 | 62.67 |
| **7** | 8.26 | 40.30 |
| **8** | 10.05 | 58.76 |
| **9** | 9.06 | 60.75 |
| **10** | 12.20 | 72.02 |
| **11** | 10.10 | 63.45 |
| **12** | 9.04 | 53.08 |
| **13** | 8.05 | 50.70 |
| **14** | 7.04 | 57.30 |
| **15** | 10.22 | 62.16 |
| **16** | 8.86 | 58.63 |
| **17** | 11.05 | 75.36 |

The correlation between flux and salt rejection suggests a trade-off between these two parameters. Membranes with higher flux often exhibited lower salt rejection, and vice versa. This observation is consistent with the findings of Zhou *et al*. [19], who reported that incorporating MWCNTs and $SiO_2$ into PVDF membranes improved flux at the expense of some salt rejection due to increased pore size. The optimal membrane (Run 17) appears to represent a balanced compromise between flux and salt rejection, achieving moderate performance in both parameters. This trade-off is well documented in the membrane distillation literature, where increasing porosity and pore size enhance flux but can compromise salt rejection if pore wetting occurs [9].

### 3.7 Total Porosity

The total porosity analysis revealed that the XTCS membrane (MWCNT/$SiO_2$/ECH-PVDF) exhibited a porosity of 56.60 %, while the TCS membrane (MWCNT/$SiO_2$/ECH/TCS-PVDF) showed a significantly higher porosity of 82.40 %. This substantial increase indicates that the TCS coating effectively introduced additional void spaces or enhanced the existing pore structure. The presence of TCS may facilitate pore formation by altering thermodynamic interactions during phase inversion [44]. This finding is consistent with the observations of Sun *et al*. [29], who reported that surface coating with

* Corresponding to: R. A. Wahab (email: roswanira@utm.my)
DOI: https://doi.org/10.11113/jamst.v30n2.353

organic compounds can significantly increase membrane porosity by promoting the formation of larger pores during phase inversion. High membrane porosity, generally in the 80–90 % range, is critical for enhancing flux and energy efficiency in membrane distillation processes [33, 48]. The MWCNT/$SiO_2$/ECH/TCS-PVDF membrane, with its porosity of 82.40 %, falls within this optimal range, suggesting potential for superior flux performance. This is consistent with the high flux observed for the TCS membrane (11.05 $kg \cdot m^{-2} \cdot h^{-1}$). Despite the high porosity, salt rejection remained moderate, suggesting that pore size and distribution may also play a significant role in determining rejection efficiency [52]. The reduction in pore size observed in SEM analysis (from 432–476 nm for the XTCS membrane to 133–219 nm for the TCS membrane) may have contributed to improved salt rejection by restricting the passage of salt ions, although the achieved rejection values still fall short of the target benchmark [50].

## 3.8 Physicochemical Characterization

### *3.8.1 FTIR Spectroscopy: Attenuated Total Reflection (ATR-FTIR)*

The ATR-FTIR spectra provided evidence for the successful incorporation of the various components into the membrane structure (Figures 3a-b, Table 13). For the XTCS membrane, the broad peak at 3396.77 $cm^{-1}$ corresponds to O-H stretching vibrations, indicative of hydroxyl groups on the surface of $SiO_2$, MWCNTs, or ECH [36]. The strong peak at 1730.77 $cm^{-1}$ is characteristic of C=O stretching vibrations from ester groups, originating from the carboxylic acid functionalities on the functionalized MWCNT-COOH starting material [45], confirming the successful incorporation of MWCNT into the membrane matrix. Meanwhile, the disappearance or reduction in intensity of the O-H stretching peak upon TCS modification suggests that the hydroxyl groups on the MWCNT-ECH were consumed during the reaction with TCS, confirming the covalent attachment of TCS to the MWCNT backbone through an ether linkage [24]. The peaks at 1400.66 $cm^{-1}$ and 1275.14 $cm^{-1}$ are attributed to C-F and C-O stretching vibrations, respectively, associated with the PVDF backbone and ester groups [44]. The peak at 1070.54 $cm^{-1}$ corresponds to Si-O-Si stretching vibrations, confirming the incorporation of $SiO_2$ [53].

After TCS modification, the most significant structural changes were observed: new peaks emerged at 1639.70 $cm^{-1}$ and 1452.91 $cm^{-1}$ (C=C aromatic stretching) and at 741.70 $cm^{-1}$ (C-Cl stretching), confirming successful TCS incorporation [60]. The retention of the C=O ester peak at 1733.04 $cm^{-1}$ indicated stability of the MWCNT functionalities, while the shift in the O-H peak to 3373.77 $cm^{-1}$ suggested consumption of hydroxyl groups during TCS attachment, consistent with covalent bond formation between TCS and MWCNT-ECH [24]. These findings align with previous reports on TCS-functionalized membranes [23, 60] and collectively confirm the successful fabrication of the MWCNT/$SiO_2$/ECH/TCS-PVDF composite.

* Corresponding to: R. A. Wahab (email: roswanira@utm.my)
DOI: https://doi.org/10.11113/jamst.v30n2.353

a)

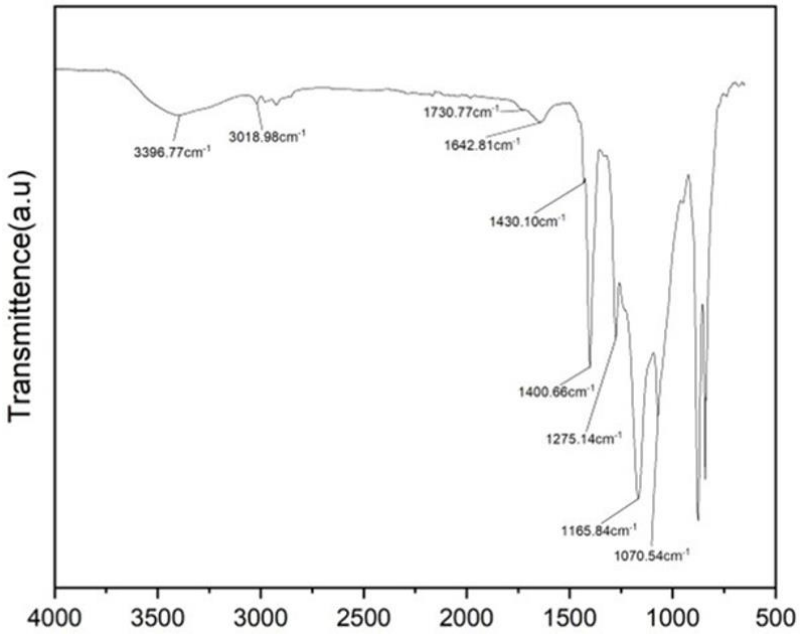


b)

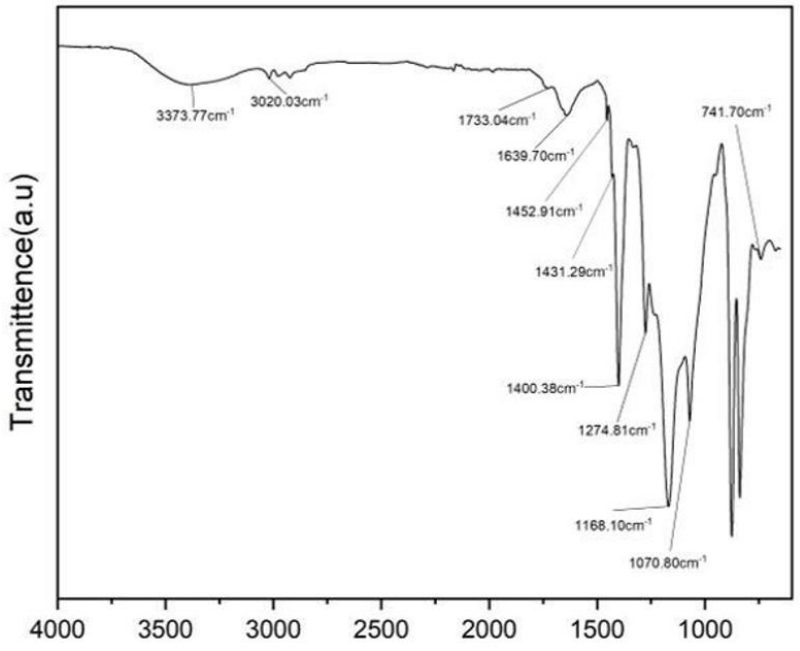


**Figure 3**. The FTIR spectra for the a) MWCNT/$SiO_2$/ECH-PVDF and b) MWCNT/$SiO_2$/ECH/TCS-PVDF membranes

* Corresponding to: R. A. Wahab (email: roswanira@utm.my)
DOI: https://doi.org/10.11113/jamst.v30n2.353

**Table 13**. ATR-FTIR frequency table for (a) the MWCNT/$SiO_2$/ECH-PVDF membrane and (b) the MWCNT/$SiO_2$/ECH/TCS-PVDF membrane

| Frequency ($cm^{-1}$) | | Functional group |
|---|---|---|
| a) | 3396.77 | O-H |
| | 1730.77 | C=O ester C-F (pvdf) |
| 1400.66 | | C-O ester Si-O-Si |
| 1275.14 | | |
| 1070.54 | | |
| b) | 3373.77 | O-H |
| | 1733.04 | C=O ester C-O ester |
| 1274.81 | | C-F |
| 1400.38 | | Si-O-Si |
| 1070.80 | | C=C aromatic C-Cl |
| 1639.70, 1452.91 | | |
| 741.70 | | |

The disappearance or reduction in intensity of the O-H stretching peak upon TCS modification suggests that the hydroxyl groups on the MWCNT-ECH were consumed during the esterification reaction with TCS, confirming the covalent attachment of TCS to the MWCNT backbone [24]. This is further supported by the presence of aromatic C=C peaks, characteristic of the phenolic structure of TCS [60]. Overall, the ATR-FTIR analysis confirms the successful functionalization of MWCNT with ECH and TCS, as well as the incorporation of $SiO_2$ and PVDF in the composite membrane.

### 3.9 Scanning Electron Microscope

The SEM micrographs provided detailed information on the cross-sectional and surface morphology of the membranes. The cross-sectional images (Figures 4a-b) showed that the XTCS membrane had a thickness of approximately 99.15 µm, while the TCS membrane exhibited a slightly reduced thickness of 82.75 µm. The reduction in thickness suggests that TCS coating may have induced some densification or restructuring of the membrane [13]. The cross-sectional structure of the TCS membrane appeared more defined, with distinct layers, indicating a more compact and potentially more robust structure, which is favorable for enhancing mechanical stability in DCMD applications [51]. Previous studies have shown that membranes with thicknesses of 30–60 µm are generally recommended for DCMD applications; however, under high-salinity conditions, thicker membranes may be preferred to enhance performance [33, 48].

* Corresponding to: R. A. Wahab (email: roswanira@utm.my)
DOI: https://doi.org/10.11113/jamst.v30n2.353

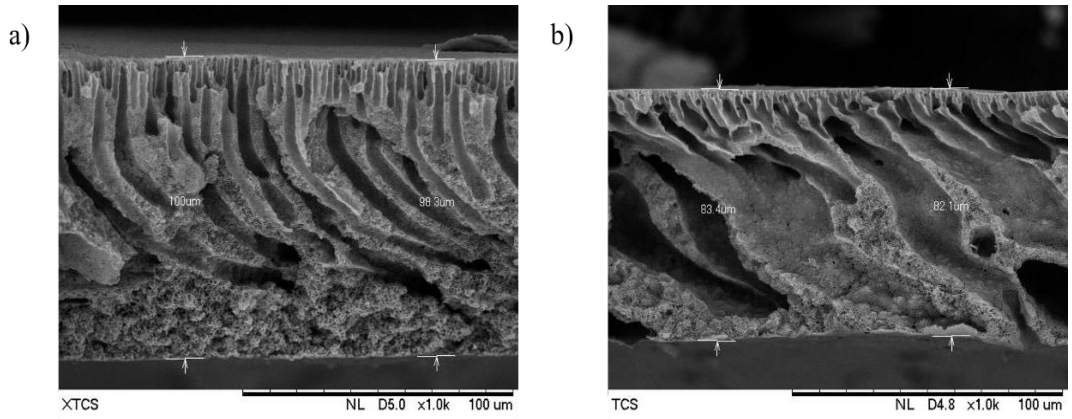


**Figure 4.** The SEM micrographs of the cross-section for (a) the MWCNT/$SiO_2$/ECH-PVDF membrane and (b) the MWCNT/$SiO_2$/ECH/TCS-PVDF membrane

The surface morphology images (Figure 5) showed that the XTCS membrane exhibited a relatively uniform surface with minor roughness and pore sizes ranging from 432 nm to 476 nm. The TCS membrane showed a denser network of smaller pores, with pore sizes ranging from 133 nm to 219 nm. The reduction in pore size is beneficial for improving salt rejection efficiency, as smaller pores are less likely to allow salt ions to pass [50]. This is consistent with the higher salt rejection observed for the TCS membrane compared to the XTCS membrane. However, the pores in the TCS membrane appeared less uniformly distributed, which may contribute to performance variability. This non-uniformity could be attributed to uneven TCS deposition or incomplete mixing during the coating process [22].

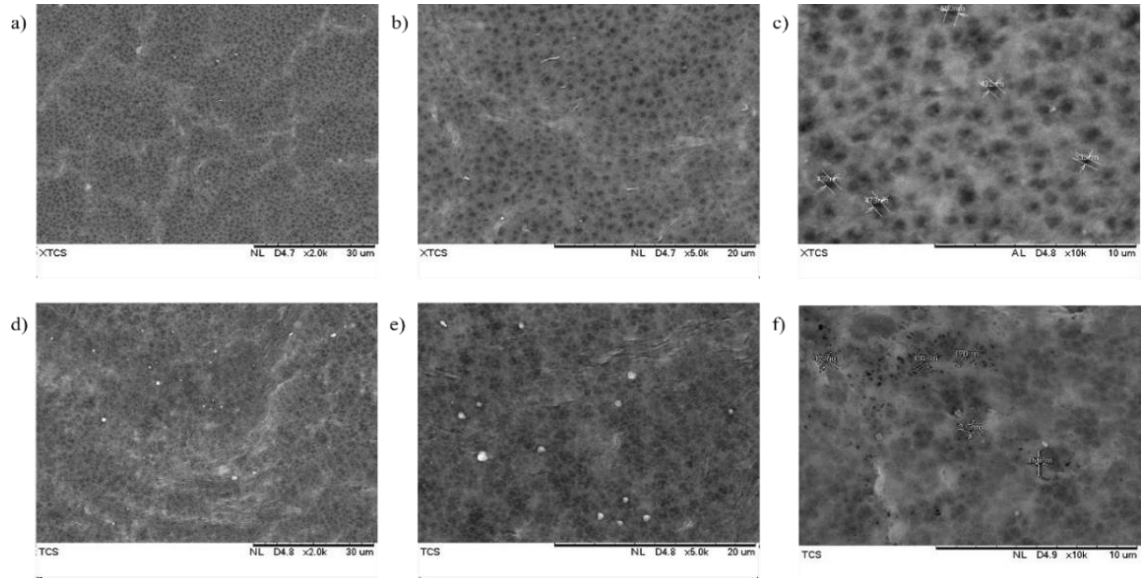


**Figure 5.** The SEM micrographs of the MWCNT/$SiO_2$/ECH-PVDF (XTCS) and MWCNT/$SiO_2$/ECH/TCS-PVDF (TCS) membrane with magnifications for (a) XTCS at 2.0k, (b)5.0k, (c) XTCS at 10.0k, as well as (d) TCS at 2.0k, (e) TCS at 5.0k and (f) TCS at 10.0k

* Corresponding to: R. A. Wahab (email: roswanira@utm.my)
DOI: https://doi.org/10.11113/jamst.v30n2.353

The white crystals observed on the TCS membrane surface (Figure 5f) are likely undissolved TCS, indicating incomplete dissolution during the coating process [23]. These crystals may impact the membrane's surface properties, potentially affecting hydrophobicity and overall performance. This observation highlights the need for improved TCS dispersion strategies to achieve uniform coating and consistent performance [20]. Strategies such as using a cosolvent, increasing the dissolution temperature, or employing ultrasonication could improve the homogeneity of the TCS solution and reduce crystal formation [7]. Additionally, the surface morphology of the TCS membrane appeared rougher than that of the XTCS membrane, likely due to the deposition of TCS particles on its surface. Increased surface roughness can enhance hydrophobicity by increasing the air-solid interface area, as described by the Cassie-Baxter model [38]. This is consistent with the improved contact angles observed for some TCS-coated membranes (e.g., Membranes 5 and 17). However, the presence of TCS crystals may create defects that compromise the uniform roughness required for optimal hydrophobicity.

The presence of undissolved TCS crystals on the membrane surface (Figure 5f) is a critical observation that helps explain, in part, the moderate salt rejection observed in this study. These crystals likely create localized defects in the hydrophobic surface, providing pathways for liquid penetration and pore wetting [23]. Previous studies have shown that uniform distribution of hydrophobic agents is essential for maintaining the integrity of the vapor-liquid interface [7, 58]. The incomplete dissolution of TCS during the coating process, possibly due to the limited solubility of TCS in Tris buffer at pH 8.5 [60], suggests that alternative coating strategies, such as using organic cosolvents, increasing the dissolution temperature, or employing ultrasonication, could improve TCS dispersion and coating uniformity [22]. Additionally, the non-uniform pore distribution observed in the TCS membrane (Figure 5d-f) may contribute to performance variability, as regions with larger pores are more susceptible to wetting [50].

## 4.0 CONCLUSION

The MWCNT/$SiO_2$/ECH/TCS-PVDF membrane was successfully fabricated, and the optimal formulation was identified as 2 wt.% ECH, 1 wt.% TCS, and 2 wt.% $SiO_2$. This formulation yielded a contact angle of 92.98°, a water flux of 11.05 $kg \cdot m^{-2} \cdot h^{-1}$, and a salt rejection rate of 75.36 %. The ATR-FTIR analysis confirmed the presence of characteristic functional groups for MWCNT (C=O ester bond at 1733.04 $cm^{-1}$), TCS (C=C aromatic at 1639.70 $cm^{-1}$ and 1452.91 $cm^{-1}$), and $SiO_2$ (Si-O-Si bond at 1070.80 $cm^{-1}$), confirming successful incorporation of all components. SEM analysis revealed a reduction in pore size from 432–476 nm to 133–219 nm upon TCS coating, which is beneficial for salt rejection. The total porosity was 82.40 % for the TCS membrane, indicating a highly porous structure suitable for MD applications. The RSM-BBD optimisation successfully identified the optimal formulation and provided statistical models for predicting membrane performance. The significant parameters influencing the responses were identified, with $SiO_2$ concentration being the most influential factor for all three responses. The models for salt rejection and water flux showed reasonable fit, while the contact angle model requires further refinement. However, the salt rejection achieved (75.36%) is substantially below the >99% benchmark required for practical DCMD applications, and the contact angle (92.98°) falls well short of the superhydrophobic threshold (>150°). These limitations are attributed to insufficient hydrophobicity to maintain a stable Cassie-Baxter state, non-uniform TCS deposition creating surface defects, and potential pore wetting during

* Corresponding to: R. A. Wahab (email: roswanira@utm.my)
DOI: https://doi.org/10.11113/jamst.v30n2.353

operation. These findings indicate that while the dual-functional approach shows promise, significant improvements in surface modification strategies, including achieving uniform TCS coating, incorporating hierarchical surface structures for superhydrophobicity, and optimizing pore size distribution, are necessary before this membrane can be considered for practical desalination applications. The presence of undissolved TCS crystals observed in SEM images indicates the need for improved coating strategies to achieve uniform surface modification. Despite these limitations, the membrane shows potential for DCMD application, and the findings provide a foundation for future work aimed at developing high-performance, anti-biofouling membranes for water desalination.

The practical significance of this work lies in establishing a foundational framework for the systematic optimization of PVDF-based membranes with MWCNT, $SiO_2$, and TCS. While the current performance metrics (75.36% salt rejection, 92.98° contact angle) fall short of industrial benchmarks for DCMD, the identification of $SiO_2$ concentration as the most influential factor, the achievement of 82.40% porosity, and the successful covalent integration of TCS confirmed by ATR-FTIR provide a solid basis for future research. Key directions for improvement include: (1) optimizing TCS dispersion and coating uniformity to eliminate crystal formation and achieve consistent surface modification; (2) incorporating hierarchical surface structures (e.g., electrospun nanofibers or lotus-leaf mimics) to achieve superhydrophobicity; and (3) exploring alternative cross-linking agents or reaction conditions to enhance the covalent attachment of TCS. With these refinements, the dual-functional approach demonstrated in this work holds promise for developing high-performance, anti-biofouling membranes for sustainable water desalination.

## DECLARATION OF COMPETING INTEREST

The authors declare that they have no known competing financial interests or personal relationships that could have appeared to influence the work reported in this paper.

## ACKNOWLEDGEMENT

The authors would like to thank the Department of Chemistry, the Faculty of Science for their facilities. This work was funded by the HICOE Research Grant (R.J090301.7854.4J524) awarded by the Ministry of Higher Education of Malaysia.

## REFERENCES

[1] Salehi, M. (2022). Global water shortage and potable water safety; Today's concern and tomorrow's crisis. *Environment International, 158*, 106936. https://doi.org/10.1016/j.envint.2021.106936

[2] World Health Organization. (2019). Progress on household drinking water, sanitation and hygiene 2000-2017: Special focus on inequalities. World Health Organization.

[3] Camacho, L. M., Dumée, L., Zhang, J., Li, J. D., Duke, M., Gomez, J. and Gray, S. (2013). Advances in membrane distillation for water desalination and purification applications. *Water, 5*(1), 94-196. https://doi.org/10.3390/w5010094

[4] Deshmukh, A., Boo, C., Karanikola, V., Lin, S., Straub, A.P., Tong, T., Warsinger, D. M. and Elimelech, M. (2018). Membrane distillation at the water-energy nexus:

* Corresponding to: R. A. Wahab (email: roswanira@utm.my)
DOI: https://doi.org/10.11113/jamst.v30n2.353

Limits, opportunities, and challenges. *Energy & Environmental Science*, *11*(5), 1177-1196. https://doi.org/10.1039/C8EE00291F

[5] Ashoor, B., Mansour, S., Giwa, A., Dufour, V. and Hasan, S. (2016). Principles and applications of direct contact membrane distillation (DCMD): A comprehensive review. *Desalination, 398*, 222-246. https://doi.org/10.1016/j.desal.2016.07.043

[6] Yao, M., Tijing, L. D., Naidu, G., Kim, S.H., Matsuyama, H., Fane, A. G. and Shon, H. K. (2020). A review of membrane wettability for the treatment of saline water deploying membrane distillation. *Desalination, 479*, 114312. https://doi.org/10.1016/j.desal.2020.114312

[7] Samadi, A., Ni, T., Fontananova, E., Tang, G., Shon, H. and Zhao, S. (2023). Engineering antiwetting hydrophobic surfaces for membrane distillation: A review. *Desalination, 563*, 116722. https://doi.org/10.1016/j.desal.2023.116722

[8] Chang, H., Liu, B., Zhang, Z., Pawar, R., Yan, Z., Crittenden, J. C. and Vidic, R. D. (2020). A critical review of membrane wettability in membrane distillation from the perspective of interfacial interactions. *Environmental Science & Technology, 55*(3), 1395-1418. https://doi.org/10.1021/acs.est.0c05454

[9] Goh, S., Zhang, J., Liu, Y. and Fane, A.G. (2013). Fouling and wetting in membrane distillation (MD) and MD-bioreactor (MDBR) for wastewater reclamation. *Desalination, 323*, 39-47. https://doi.org/10.1016/j.desal.2012.12.001

[10] AlSawaftah, N., Abuwatfa, W., Darwish, N. and Husseini, G. (2021). A comprehensive review on membrane fouling: Mathematical modelling, prediction, diagnosis, and mitigation. *Water, 13*(9), 1327. https://doi.org/10.3390/w13091327

[11] Zahid, M., Khalid, T., Rehan, Z.A., Javed, T., Akram, S., Rashid, A., Mustafa, S.K., Shabbir, R., Mora-Poblete, F., Asad, M.S., Liaquat, R., Hassan, M.M., Amin, M.A. and Shakoor, H.A. (2021). Fabrication and characterization of sulfonated graphene oxide (SGO) doped PVDF nanocomposite membranes with improved anti-biofouling performance. *Membranes, 11*(10), 749. https://doi.org/10.3390/membranes11100749

[12] Hang, M., Liao, B.Q., Zhou, X., He, Y., Hong, H., Lin, H. and Chen, J. (2015). Effects of hydrophilicity/hydrophobicity of membrane on membrane fouling in a submerged membrane bioreactor. *Bioresource Technology, 175,* 59-67. https://doi.org/10.1016/j.biortech.2014.10.058

[13] Zhang, J., Song, Z., Li, B., Wang, Q. and Wang, S. (2013). Fabrication and characterization of superhydrophobic poly (vinylidene fluoride) membrane for direct contact membrane distillation. *Desalination, 324,* 1-9. https://doi.org/10.1016/j.desal.2013.05.018

[14] Nthunya, L. N., Gutierrez, L., Derese, S., Nxumalo, E. N., Verliefde, A. R., Mamba, B. B. and Mhlanga, S. D. (2019). A review of nanoparticle-enhanced membrane distillation membranes: Membrane synthesis and applications in water treatment. *Journal of Chemical Technology & Biotechnology, 94*(9), 2757-2771. https://doi.org/10.1002/jctb.5977

[15] Wu, X., Zhao, B., Wang, L., Zhang, Z., Li, J., He, X., Zhang, H., Zhao, X. and Wang, H. (2018). Superhydrophobic PVDF membrane induced by hydrophobic SiO2 nanoparticles and its use for $CO_2$ absorption. *Separation and Purification Technology, 190*, 108-116. https://doi.org/10.1016/j.seppur.2017.07.076

[16] Tijing, L. D., Woo, Y. C., Shim, W. G., He, T., Choi, J.S., Kim, S. H. and Shon, H.

* Corresponding to: R. A. Wahab (email: roswanira@utm.my)
DOI: https://doi.org/10.11113/jamst.v30n2.353

K. (2016). Superhydrophobic nanofiber membrane containing carbon nanotubes for high-performance direct contact membrane distillation. *Journal of Membrane Science, 502*, 158-170. https://doi.org/10.1016/j.memsci.2015.12.014

[17] Jamed, M. J., Alhathal Alanezi, A. and Alsalhy, Q. F. (2019). Effects of embedding functionalized multi-walled carbon nanotubes and alumina on the direct contact poly (vinylidene fluoride-co-hexafluoropropylene) membrane distillation performance. *Chemical Engineering Communications, 206*(8), 1035-1057. https://doi.org/10.1080/00986445.2018.1542302

[18] Silva, T. L. S., Morales-Torres, S., Figueiredo, J. L. and Silva, A. M. T. (2015). Multi-walled carbon nanotube/PVDF blended membranes with sponge- and finger-like pores for direct contact membrane distillation. *Desalination, 357*, 233-245. https://doi.org/10.1016/j.desal.2014.11.025

[19] Zhou, R., Rana, D., Matsuura, T. and Lan, C.Q. (2019). Effects of multi-walled carbon nanotubes (MWCNTs) and integrated MWCNTs/SiO2 nano-additives on PVDF polymeric membranes for vacuum membrane distillation. *Separation and Purification Technology, 217*, 154-163. https://doi.org/10.1016/j.seppur.2019.02.013

[20] Feng, X., Guo, W., Zheng, H., Yang, S., Du, J., Wu, Q., Luo, H., Zhou, X., Jin, W. and Ren, N. (2020). Inhibition of biofouling in membrane bioreactor by metabolic uncoupler based on controlling microorganisms accumulation and quorum sensing signals secretion. *Chemosphere, 245,* 125363. https://doi.org/10.1016/j.chemosphere.2019.125363

[21] Shrestha, P., Ni, J. and Wong, T.Y. (2020). Synergistic and antagonistic interactions of triclosan with various antibiotics in bacteria. *Journal of Environmental Science and Health, Part C, 38*(3), 187-203. https://doi.org/10.1080/26896583.2020.1781494

[22] Tang, Z. W., Ma, C. Y., Wu, H. X., Tan, L., Xiao, J. Y., Zhuo, R. X. and Liu, C. J. (2016). Antiadhesive zwitterionic poly-(sulphobetaine methacrylate) brush coating functionalized with triclosan for high-efficiency antibacterial performance. *Progress in Organic Coatings, 97,* 277-287. https://doi.org/10.1016/j.porgcoat.2016.04.038

[23] Park, S. H., Hwang, S. O., Kim, T. S., Cho, A., Kwon, S. J., Kim, K. T., Park, H. D. and Lee, J. H. (2018). Triclosan-immobilized polyamide thin film composite membranes with enhanced biofouling resistance. *Applied Surface Science, 443*, 458-466. https://doi.org/10.1016/j.apsusc.2018.03.003

[24] Yusmaidi, N., Abdul Wahab, R., W. J. Lau, Mohammed Al-Fakih, A. and Wayan Adnyana, B. (2026). Improved simultaneous antibacterial and filtration by novel Triclosan-functionalized multi-walled carbon nanotubes/polyvinylidene fluoride ultrafiltration membrane. *Journal of Industrial and Engineering Chemistry*.

[25] Boubakri, A., Bouguecha, S. A. T. and Hafiane, A. (2021). Box–Behnken design assisted by theoretical mass and heat transfer using for multi-responses optimization of membrane distillation process. *Chemical Papers, 75*(11), 6009-6024. https://doi.org/10.1007/s11696-021-01778-6

[26] Ferreira, S. C., Bruns, R., Ferreira, H. S., Matos, G. D., David, J., Brandão, G., da Silva, E. P., Portugal, L., Dos Reis, P. and Souza, A. (2007). Box-Behnken design: An alternative for the optimization of analytical methods. *Analytica Chimica Acta, 597*(2), 179-186. https://doi.org/10.1016/j.aca.2007.07.011

* Corresponding to: R. A. Wahab (email: roswanira@utm.my)
DOI: https://doi.org/10.11113/jamst.v30n2.353

[27] Gontarek-Castro, E., Castro-Muñoz, R., & Lieder, M. (2022). New insights of nanomaterials usage toward superhydrophobic membranes for water desalination via membrane distillation: A review. *Critical Reviews in Environmental Science and Technology*, *52*(12), 2104-2149.
[28] Silva, T. L. S., Morales-Torres, S., Figueiredo, J. L., & Silva, A. M. T. (2015). Multi-walled carbon nanotube/PVDF blended membranes with sponge- and finger-like pores for direct contact membrane distillation. *Desalination*, *357*, 233-245.
[29] Sun, W., Shen, F., Wang, Z., Zhang, Y., & Wan, Y. (2018). An ultrathin, porous and in-air hydrophilic/underwater oleophobic coating simultaneously increasing the flux and antifouling property of membrane for membrane distillation. *Desalination*, *445*, 40-50.
[30] Ferreira, S. C., Bruns, R., Ferreira, H. S., Matos, G. D., David, J., Brandão, G., *et al.* (2007). Box-Behnken design: An alternative for the optimization of analytical methods. *Analytica Chimica Acta*, *597*(2), 179-186.
[31] Montgomery, D. C. (2017). *Design and Analysis of Experiments* (9th ed.). John Wiley & Sons.
[32] Boubakri, A., Bouguecha, S. A. T., & Hafiane, A. (2021). Box–Behnken design assisted by theoretical mass and heat transfer using for multi-responses optimization of membrane distillation process. *Chemical Papers*, *75*(11), 6009-6024.
[33] Eykens, L., De Sitter, K., Dotremont, C., Pinoy, L., & Van der Bruggen, B. (2016). Characterization and performance evaluation of commercially available hydrophobic membranes for direct contact membrane distillation. *Desalination*, *392*, 63-73.
[34] Kong, S., Lim, M.-y., Shin, H., Baik, J.-H., & Lee, J.-C. (2020). High-flux and antifouling polyethersulfone nanocomposite membranes incorporated with zwitterion-functionalized graphene oxide for ultrafiltration applications. *Journal of Industrial and Engineering Chemistry*, *84*, 131-140.
[35] AbdulKadir, W. A. F. W., Ahmad, A. L., Seng, O. B., & Lah, N. F. C. (2020). Biomimetic hydrophobic membrane: A review of anti-wetting properties as a potential factor in membrane development for membrane distillation (MD). *Journal of Industrial and Engineering Chemistry*, *91*, 15-36.
[36] Alizadeh, A., Razmjou, A., Ghaedi, M., & Jannesar, R. (2019). Nanoporous solid-state membranes modified with multi-wall carbon nanotubes with anti-biofouling property. *International Journal of Nanomedicine*, *14*, 1669-1685.
[37] Boubakri, A., Bouguecha, S.A.T., & Hafiane, A. (2021). Box–Behnken design assisted by theoretical mass and heat transfer using for multi-responses optimization of membrane distillation process. *Chemical Papers*, *75*(11), 6009-6024.
[38] Cassie, A. B. D., & Baxter, S. (1944). Wettability of porous surfaces. *Transactions of the Faraday Society*, *40*, 546-551.
[39] Chang, H., Liu, B., Zhang, Z., Pawar, R., Yan, Z., Crittenden, J.C., & Vidic, R. D. (2020). A critical review of membrane wettability in membrane distillation from the perspective of interfacial interactions. *Environmental Science & Technology*, *55*(3), 1395-1418.
[40] Chen, L., Xu, P., & Wang, H. (2020). Interplay of the factors affecting water flux and salt rejection in membrane distillation: A state-of-the-art critical review. *Water*, *12*(10), 2841.

* Corresponding to: R. A. Wahab (email: roswanira@utm.my)
DOI: https://doi.org/10.11113/jamst.v30n2.353

[41] Devi, S., Ray, P., Singh, K., & Singh, P. S. (2014). Preparation and characterization of highly micro-porous PVDF membranes for desalination of saline water through vacuum membrane distillation. *Desalination*, *346*, 9-18.
[42] Dumée, L., Campbell, J.L., Sears, K., Schütz, J., Finn, N., Duke, M., & Gray, S. (2011). The impact of hydrophobic coating on the performance of carbon nanotube bucky-paper membranes in membrane distillation. *Desalination*, *283,* 64-67.
[43] Eykens, L., De Sitter, K., Dotremont, C., Pinoy, L., & Van der Bruggen, B. (2016). Characterization and performance evaluation of commercially available hydrophobic membranes for direct contact membrane distillation. *Desalination*, *392*, 63-73.
[44] Fahrina, A., Arahman, N., Mulyati, S., Aprilia, S., Mat Nawi, N. I., Aqsha, A., Bilad, M. R., Takagi, R., & Matsuyama, H. (2020). Development of polyvinylidene fluoride membrane by incorporating bio-based ginger extract as additive. *Polymers*, *12*(9), 2003.
[45] Farid, M. U., Khanzada, N. K., & An, A. K. (2019). Understanding fouling dynamics on functionalized CNT-based membranes: Mechanisms and reversibility. *Desalination*, *456*, 74-84.
[46] Feng, X., Guo, W., Zheng, H., Yang, S., Du, J., Wu, Q., Luo, H., Zhou, X., Jin, W., & Ren, N. (2020). Inhibition of biofouling in membrane bioreactor by metabolic uncoupler based on controlling microorganisms accumulation and quorum sensing signals secretion. *Chemosphere*, *245*, 125363.
[47] Ferreira, S. C., Bruns, R., Ferreira, H. S., Matos, G. D., David, J., Brandão, G., *et al.* (2007). Box-Behnken design: An alternative for the optimization of analytical methods. *Analytica Chimica Acta*, *597*(2), 179-186.
[48] Goh, S., Zhang, J., Liu, Y., & Fane, A. G. (2013). Fouling and wetting in membrane distillation (MD) and MD-bioreactor (MDBR) for wastewater reclamation. *Desalination*, *323*, 39-47.
[49] Gontarek-Castro, E., Castro-Muñoz, R., & Lieder, M. (2022). New insights of nanomaterials usage toward superhydrophobic membranes for water desalination via membrane distillation: A review. *Critical Reviews in Environmental Science and Technology*, *52*(12), 2104-2149.
[50] Guo, D., Zhang, X., Xie, J., & Li, N. (2023). Effect of cross-linking agent concentration on adsorption performance of PVDF ultrafiltration membrane. *European Polymer Journal*, *198*, 112332.
[51] Hou, D., Fan, H., Jiang, Q., Wang, J., & Zhang, X. (2014). Preparation and characterization of PVDF flat-sheet membranes for direct contact membrane distillation. *Separation and Purification Technology*, *135,* 211-222.
[52] Hsu, M.-H., Tsou, T.-Y., Hsu, J.-P., & Yu, H.-Y. (2024). Influence of pore size distribution and applied cross-flow on ion rejection and separation. *Separation and Purification Technology*, *128248*.
[53] Jamed, M. J., Alhathal Alanezi, A., & Alsalhy, Q. F. (2019). Effects of embedding functionalized multi-walled carbon nanotubes and alumina on the direct contact poly (vinylidene fluoride-co-hexafluoropropylene) membrane distillation performance. *Chemical Engineering Communications*, *206*(8), 1035-1057.
[54] Lalia, B.S., Kochkodan, V., Hashaikeh, R., & Hilal, N. (2013). A review on membrane fabrication: Structure, properties and performance relationship. *Desalination*, *326*, 77-95.

* Corresponding to: R. A. Wahab (email: roswanira@utm.my)
DOI: https://doi.org/10.11113/jamst.v30n2.353

[55] Latthe, S.S., Terashima, C., Nakata, K., & Fujishima, A. (2014). Superhydrophobic surfaces developed by mimicking hierarchical surface morphology of lotus leaf. *Molecules*, *19*(4), 4256-4283.
[56] Li, J., Xu, S., Hassan, M., Shao, J., Ren, L.F., & He, Y. (2019). Effective modeling and optimization of PVDF–PTFE electrospinning parameters and membrane distillation process by response surface methodology. *Journal of Applied Polymer Science*, *136*(9), 47125.
[57] Liao, Y., Wang, R., & Fane, A.G. (2014). Fabrication of bioinspired composite nanofiber membranes with robust superhydrophobicity for direct contact membrane distillation. *Environmental Science & Technology*, *48*(11), 6335-6341.
[58] Liu, Y., Li, K., & Wang, R. (2021). Superhydrophobic PVDF membranes for membrane distillation: A comprehensive review. *Desalination*, *512*, 115135.
[59] Montgomery, D.C. (2017). *Design and Analysis of Experiments* (9th ed.). John Wiley & Sons.
[60] Orhan, M. (2020). Triclosan applications for biocidal functionalization of polyester and cotton surfaces. *Journal of Engineered Fibers*.

* Corresponding to: R. A. Wahab (email: roswanira@utm.my)
DOI: https://doi.org/10.11113/jamst.v30n2.353